MICROCOPY RESOLUTION TEST CHART

NATIONAL BUREAU OF STANDARDS

AD-A179 297

SPECIAL EFFECT VULNERABILITY AND HARDENING PROGRAM, FINAL REPORT
Volume II—Random Imperfections for Dynamic Pulse Buckling

Herbert E. Lindberg
APTEK, Inc.
4340 Stevens Creek Blvd.
Suite 145
San Jose, CA 95129

27 December 1985

Technical Report

DTIC
ELECTE
APR 2 1 1987
E

Prepared for
    Director
    DEFENSE NUCLEAR AGENCY
    Washington, DC 20305-1000

DISTRIBUTION LIST UPDATE

This mailer is provided to enable DNA to maintain current distribution lists for reports. We would appreciate your providing the requested information.

☐ Add the individual listed to your distribution list.

☐ Delete the cited organization/individual.

☐ Change of address.

NAME: _____

ORGANIZATION: _____

OLD ADDRESS	**CURRENT ADDRESS**
_____	_____
_____	_____
_____	_____

TELEPHONE NUMBER: ( ) _____

SUBJECT AREA(s) OF INTEREST:

_____	_____
_____	_____
_____	_____

DNA OR OTHER GOVERNMENT CONTRACT NUMBER: _____

CERTIFICATION OF NEED-TO-KNOW BY GOVERNMENT SPONSOR (if other than DNA):

SPONSORING ORGANIZATION: _____

CONTRACTING OFFICER OR REPRESENTATIVE: _____

SIGNATURE: _____

Director
Defense Nuclear Agency
ATTN: STTI
Washington, DC 20305-1000

Director
Defense Nuclear Agency
ATTN: STTI
Washington, DC 20305-1000

REPORT DOCUMENTATION PAGE

Form Approved
OMB No 0704-0188
Exp Date Jun 30, 1986

1a REPORT SECURITY CLASSIFICATION	1b RESTRICTIVE MARKINGS
UNCLASSIFIED	

2a SECURITY CLASSIFICATION AUTHORITY	3 DISTRIBUTION AVAILABILITY OF REPORT
N/A since Unclassified	Approved for public release; distribution is unlimited.
2b DECLASSIFICATION DOWNGRADING SCHEDULE	
N/A since Unclassified	

4 PERFORMING ORGANIZATION REPORT NUMBER(S)	5 MONITORING ORGANIZATION REPORT NUMBER(S)
A-85-8R, Vol II (A720)	DNA-TR-86-37-V2

6a NAME OF PERFORMING ORGANIZATION	6b OFFICE SYMBOL (If applicable)	7a NAME OF MONITORING ORGANIZATION
APTEK, Inc.		Director Defense Nuclear Agency

6c ADDRESS (City, State, and ZIP Code)	7b ADDRESS (City, State, and ZIP Code)
4340 Stevens Creek Blvd. Suite 145 San Jose, CA 95129	Washington, DC 20305-1000

8a NAME OF FUNDING SPONSORING ORGANIZATION	8b OFFICE SYMBOL (If applicable)	9 PROCUREMENT INSTRUMENT IDENTIFICATION NUMBER
		DNA 001-83-C-0139

8c ADDRESS (City, State, and ZIP Code)	10 SOURCE OF FUNDING NUMBERS			
	PROGRAM ELEMENT NO	PROJECT NO	TASK NO	WORK UNIT ACCESSION NO
	62715H	N99QAXA N99QMXA	K K	DH006799

11 TITLE (Include Security Classification)
SPECIAL EFFECT VULNERABILITY AND HARDENING PROGRAM, FINAL REPORT
Volume II—Random Imperfections for Dynamic Pulse Buckling

12 PERSONAL AUTHOR(S)
Lindberg, Herbert E.

13a TYPE OF REPORT	13b TIME COVERED	14 DATE OF REPORT (Year, Month, Day)	15 PAGE COUNT
Technical	FROM 850101 TO 850901	851227	54

16 SUPPLEMENTARY NOTATION
This work was sponsored by the Defense Nuclear Agency under RDT&E RMSS Codes B342083466
N99QAXAK00039 H2590D and B342084464 N99QMXAK00019 H2590D.

17 COSATI CODES			18 SUBJECT TERMS (Continue on reverse if necessary and identify by block number)		
FIELD	GROUP	SUB-GROUP	Buckle Amplitudes	Dynamic	Monte Carlo Statistics
20	11		Buckle Shapes	Imperfections	Random
13	13		Buckling	Impulsive Loads	Shells

19 ABSTRACT (Continue on reverse if necessary and identify by block number)
→Pure white noise and wavelength-dependent random imperfections are explored as
representations of imperfections to be used in numerical investigation of dynamic pulse
buckling. Both forms provide imperfections with a broad spectrum of wavelengths, which is
needed to allow the numerical analysis to select the most amplified wavelengths as part of
the solution. Example results from a closed form solution are used to show how these
imperfections are related to equivalent single-mode imperfections and to demonstrate the
statistics of typical buckled forms.

Both random imperfection forms are represented by Fourier series with random
coefficients having a Gaussian distribution with zero mean value. In white noise, the
standard deviation is constant for all wavelengths. The proposed alternate form has
standard deviations that decrease as $n^{-\frac{1}{2}}$ with increasing mode number n. This *gray noise*
is a convenient form that is shown to represent imperfections that are proportional to an
appropriate combination of wall thickness and wavelengths of the buckle modes.

20 DISTRIBUTION AVAILABILITY OF ABSTRACT			21 ABSTRACT SECURITY CLASSIFICATION
☐ UNCLASSIFIED UNLIMITED	☒ SAME AS RPT	☐ DTIC USERS	UNCLASSIFIED

22a NAME OF RESPONSIBLE INDIVIDUAL	22b TELEPHONE (Include Area Code)	22c OFFICE SYMBOL
Betty L. Fox	(202) 325-7042	DNA/STTI

DD FORM 1473, 84 MAR
83 APR edition may be used until exhausted
All other editions are obsolete

SECURITY CLASSIFICATION OF THIS PAGE
UNCLASSIFIED

19. ABSTRACT (Continued)

Example random imperfection shapes and growing buckle shapes are given to demonstrate the advantage of using gray-noise rather than pure white-noise imperfections. In addition, distributions of peak-to-peak buckle amplitudes and buckle wavelengths are calculated by the Monte Carlo method for a large population of random buckle shapes. It is shown that estimates of the statistics of these distributions can be made to reasonable accuracy by a single calculation in which about 15 or more buckle waves appear. This is an important result for finite element calculations, in which Monte Carlo calculations would be time consuming and expensive.

Accession For	
NTIS GRA&I	X
DTIC TAB	☐
Unannounced	☐
Justification	

By		
Distribution/		
Availability Codes		
Dist	Avail and/or Special	
A-1		

Table of Contents

List of Illustrations

List of Illustrations (Concluded)

vi

Section 1

Introduction

A dominant mode of response in metal cylindrical shells under impulsive pressures is dynamic pulse buckling into high order buckle modes with short wavelengths. The dominant modes typically have 20 to more than 100 waves around the circumference, depending on the material and radius-to-thickness ratio of the shell. These mode numbers must be determined as part of the solution to buckling response. In closed form analyses[1], they have been found by calculating response in a sequence of modes to find the most amplified mode. Critical impulses for threshold buckling are then estimated by representing the actual motion, which takes place in many amplified modes, by motion in only the most amplified mode[2].

With this procedure it is not necessary to provide a detailed description of the imperfections that trigger buckling. It is enough to assume that random imperfections are present in all the modes, so that the buckle motion can selectively amplify the critical mode into which the shell buckles. Imperfections are then represented by an equivalent single imperfection in this mode. However, for more complex shell geometries and loadings, solutions must be found by numerical methods. In the finite element method with the shell descritized around the circumference, some other means must be used to specify imperfections so the response analysis can yield the buckle shape and critical impulse.

---

[1] H. E. Lindberg and D. L Anderson, "Dynamic Pulse Buckling of Cylindrical Shells Under Transient Lateral Pressures," AIAA J., 6, (4), pp. 589-598, April 1968.

[2] H. E. Lindberg and A. L. Florence, *Dynamic Pulse Buckling–Theory and Experiment*, DNA 6503H, Defense Nuclear Agency Press, Washington DC, February 1983.

1

In this report, it is proposed that the imperfections be taken as a nearly white noise perturbation from a perfectly circular shape. This perturbation is described by a Fourier series with random coefficients, each having a Gaussian distribution in amplitude with zero mean value and standard deviation $\sigma(n)$. The proposed form for σ is $\sigma = Chn^{-1/2}$, where C is a parameter determined in the report by comparison with experimental results and h is wall thickness. This form of departure from true white noise, in which σ is constant for all wave numbers, is shown to describe imperfections that are proportional to an appropriate combination of the wall thickness and the wavelength of each buckling mode.

This specification gives imperfection coefficients that decrease conservatively slowly with increasing n as compared with measurements on a limited number of shells, and is more physically reasonable than a pure white noise description, which gives a divergent series for the perturbation shape. The $n^{-1/2}$ decrease in standard deviation results in a nearly convergent series for the mean square deviation of the imperfection shape; the exponent $-1/2$ is the separator between convergent and divergent series.

Buckle shapes resulting from this imperfection description are calculated analytically at a sequence of increasing times. The resulting buckle shapes are compared with imperfection shapes found by truncating the imperfection series at a sequence of bandwidths ranging from a small fraction of the bandwidth of the dynamic buckling amplification function to several times this bandwidth These examples give a physical feel for the imperfection form, the nature of its convergence, and how it is modified by pulse buckling amplification.

Buckle forms are then calculated for a large number of random imperfection shapes to determine the statistics of the amplitudes and wavelengths of the buckles. It is shown that good estimates of the statistics of the universe of buckle shapes can be obtained by calculating the statistics of the buckles in a single calculation. This is an important result for use in finite element calculations, in which Monte Carlo calculations for buckle statistics would be expensive and time consuming.

2

Section 2

White Noise and Single-Mode Imperfections

2.1 Buckling from White Noise Imperfections

A mathematical analysis of random noise currents in electrical communication, described by Rice[3], is closely analogous to the analysis of buckle shapes in long shells under radial impulse uniform around the circumference. We consider a shell with a random shape imperfection given by

$$u_i(\theta) = \sum_{n=2}^{N}[\alpha_n \cos n\theta + \beta_n \sin n\theta] \qquad (2.1)$$

where θ is angle around the circumference, n is mode number, the coefficients α_n and β_n are random variables, each normally distributed with zero mean value and standard deviation σ, and N is an upper limit to be determined by the buckling analysis. For clarity, we consider first that σ is constant for all n, just as in Reference 3. This is called 'white noise,' by analogy to the electrical case in which u_i would be current and θ would be time. Example imperfection shapes from Eq. (2.1) are given in Chapter 3.

---

[3]S. O. Rice, "Mathematical Analysis of Random Noise," in *Selected Papers on Noise and Stochastic Processes*, Nelson Wax, ed., Dover Publications, New York, NY, 1954, pp. 133-294.

The resulting buckle shape is given by

$$u(\theta, \tau) = u_0(\tau) + \sum_{n=2}^{N} [a_n(\tau) \cos n\theta + b_n(\tau) \sin n\theta] \qquad (2.2)$$

where τ is a dimensionless time. The first term is the symmetric inward motion from the symmetric impulse. The remaining terms are the growing flexural modes. The term for $n = 1$ is omitted because to the accuracy of the buckling theory given in References 1 and 2 this term is a rigid body translation. Example buckle shapes from Eq. (2.2) and their growth with time are given in Chapters 3 and 4.

For the present, it is not necessary to be concerned with the details of any particular buckling analysis except for the fundamental result that the buckle shape coefficients $a_n(\tau)$ and $b_n(\tau)$ are expressed by the form

$$a_n(\tau) = \alpha_n G(n, \tau), \qquad\qquad b_n(\tau) = \beta_n G(n, \tau) \qquad (2.3)$$

where $G(n, \tau)$ is an amplification function which, at times when buckle amplitudes are observable, has significant values only over a band of modes in the range $2 < n < N$. Thus, in Eqs. (2.1) and (2.2) we have used an upper limit N because higher modes have no significant growth. This is a crucial step in specifying the imperfections in Eq. (2.1).

The mean square of the deformed shape (averaged over θ at fixed τ) is

$$\begin{aligned}
\overline{u^2}(\tau) &= \sum_{n=2}^{N} [\overline{a_n^2}(\tau) \cos^2 n\theta + \overline{b_n^2}(\tau) \sin^2 n\theta] \\
&= \sigma^2 \sum_{n=2}^{N} G^2(n, \tau) \qquad\qquad (2.4)
\end{aligned}$$

This result follows from the independence of a_n and b_n and the identity of their distributions. From the central limit theorem for the sum of many independent random variables, the distribution of u is also random normal with zero mean. This suggests that experimental determination of the mean square of the deformed buckle shape, $\overline{u^2}(\tau)$, would give a statistical description of the deformed shape.

Note that the series in Eq. (2.4) converges because of the finite bandwidth of the amplified modes. A similar series for the mean square of the initial imperfection with σ constant for all modes (white noise) does not

4

converge as $N \to \infty$. In the next chapter we suggest a physically motivated variation of σ with n that gives a convergent series for the imperfections themselves.

2.2 Specification of Random Imperfections

For finite element calculations, we propose that Eq. (2.1) be used to generate an unstressed initial deformation. The values for α_n and β_n are to be selected from a population of random numbers with zero mean value and standard deviation σ. Then the series is summed to generate $u_i(\theta)$. Element displacements are then chosen to approximate this initial shape.

We have already mentioned that to specify random imperfections in the form given by Eq. (2.1) we must specify the value of N to be used in truncating the series. In a finite element analysis, this selection goes hand in hand with the selection of the element sizes such that the buckle wavelengths can be resolved. Both depend on prior knowledge of the buckle wavelengths to be expected. The calculation itself will select the buckle wavelengths that are amplified, so one could simply take N large enough and the element size small enough to allow for any possible wavelengths. However, the time and cost of the calculation increases rapidly with the number of elements, so careful choices are necessary for N and the number of elements required to resolve the corresponding wavelength. These choices can be based on the solutions in Reference 2 for simple loading and geometry.

The other quantity to be specified is the magnitude of σ. The choice of this magnitude quantity in analogous to the choices made in Reference 2 for equivalent single-mode imperfections in the most amplified mode. In both cases, the most reasonable approach is to base the choice on observed buckle deformations rather than on an attempt to measure the actual imperfections. These imperfections are extremely small and essentially impossible to measure. Also, in practice these are 'equivalent' initial shape imperfections, that account for a range of imperfection sources, including those in wall thickness, material properties, prestresses, and so forth.

5

2.3 Relationship Between White Noise and Single-Mode Imperfections

In Reference 2 it was found that observed impulse thresholds for buckling in shells, over a range of radius-to-thickness ratios from 20 to 200, were reasonably well predicted by taking equivalent single-mode imperfections in the most amplified mode equal to 1% of the wall thickness. The critical impulses for buckling are relatively insensitive to the exact value of this imperfection because of the exponential growth of the buckles with increasing impulse.

The value to be used for σ in Eq. (2.1) can be made to correspond to this single-mode imperfection by means of the statistical analysis by Rice. Thus, for imperfections concentrated in a single mode we have

$$u_i(\theta) = \delta_n \sin n\theta \tag{2.5}$$

The buckle deformation is then simply

$$u(\theta, \tau) = \delta_n G_{\max}(\tau) \sin n\theta \tag{2.6}$$

in which $G_{\max}$ is the maximum amplification found as described above. The mean square of this deformation is

$$\begin{aligned}
\overline{u^2}(\tau) &= \delta_n^2 G_{\max}^2(\tau) \cdot \frac{1}{2\pi} \int_0^{n\theta=2\pi} \sin^2 n\theta \; d(n\theta) \\
&= \delta_n^2 G_{\max}^2(\tau) \cdot \frac{1}{2} \tag{2.7}
\end{aligned}$$

The choice for σ can now be made such that this mean square is the same as the mean square given by Eq. (2.4) for random imperfections, with the result

$$\sigma^2 \sum_{n=2}^{N} G^2(n, \tau) = \frac{\delta_n^2}{2} G_{\max}^2(\tau)$$

or

$$\sigma = \frac{\delta_n G_{\max}(\tau)}{\left[2 \sum_{n=2}^{N} G^2(n, \tau)\right]^{1/2}} \tag{2.8}$$

The above procedure assumes that the observed buckle statistic is the root mean square of the deformation. The correspondence between theory

6

and experiment in Reference 3 was actually based on the measured threshold plastic bending or plastic flow buckle deformation at the largest peaks in response. Thus, we should base the comparison between single-mode and random imperfections on the distribution of peaks rather than on the mean square deformation.

Monte Carlo calculations in Chapter 4 give the distribution of peak-to-peak amplitudes of buckle shapes. Based on this distribution, a peak value selected from a relatively large sample size (from 10 to 50 waves were typically observed in each experiment) would be equal to about three times the rms value of deformation. If we choose this value for comparison with the single-mode theory, then

$$u_{\max} = 3\sigma \left[\sum_{n=2}^{N} G^2(n, \tau) \right]^{1/2} \tag{2.9}$$

For the single-mode imperfection, $u_{\max} = \delta_n G_{\max}$. These peak deformations are equal for

$$\sigma = \frac{\delta_n G_{\max}(\tau)}{3 \left[\sum_{n=2}^{N} G^2(n, \tau) \right]^{1/2}} \tag{2.10}$$

2.4 Analytical Example

To determine the relationship between σ and δ_n according to Eq. (2.8) or (2.10), we must now specify the amplification function $G(n, \tau)$. Results given in Reference 2 demonstrate that the shape of this amplification as a function of mode number is very nearly the same for both elastic and plastic-flow buckling over a wide range of shell radius-to-thickness ratios. For our purpose here, we use the equations from plastic-flow buckling in relatively thick-walled shells, for which the amplification function is given by a simple analytic expression.

The equations of motion for this case, following an initial radial impulse uniform around the shell, were derived by Abrahamson and Goodier[4] and also in Reference 2, with the result

$$u'''' + (1 + s^2)u'' + s^2 u + \ddot{u} = -s(a/h + u_i + u_i'') \tag{2.11}$$

---

[4] G. R. Abrahamson and J. N. Goodier, "Dynamic Plastic Flow Buckling of a Cylindrical Shell from Uniform Radial Impulse," Proc. Fourth U.S. Nat. Congress of Appl. Mech., Berkeley, California, pp. 939-950, June 1962.

7

where

$$u = w/h, \qquad u_i = w_i/h, \qquad \hat{\tau} = c_p \alpha t/a \qquad (2.12)$$

$$c_p = \sqrt{E_t/\rho}, \qquad s^2 = \sigma_y/E_t\alpha^2 \qquad \alpha^2 = h^2/12a^2 \qquad (2.13)$$

in which $w(\theta, t)$ is radial deformation, positive inward, $w_i(\theta)$ is an initial unstressed imperfection shape, t is time, $\hat{\tau}$ is a dimensionless time, c_p is plastic wave speed, E_t is the material tangent modulus, assumed for now to be constant beyond yield, ρ is density, σ_y is yield stress, h is wall thickness, and a is shell radius. Note that the dimensionless displacements u and u_i are normalized by the wall thickness rather than by the radius as in References 2 and 4. Primes indicate differentiation with respect to θ and dots with respect to $\hat{\tau}$.

Substitution of the series expansions

$$u_i(\theta) = \sum_{n=2}^{N} (\alpha_n \cos n\theta + \beta_n \sin n\theta) \qquad (2.14)$$

$$u(\theta, \tau) = a_0(\tau) + \sum_{n=2}^{N} [a_n(\hat{\tau}) \cos n\theta + b_n(\hat{\tau}) \sin n\theta] \qquad (2.15)$$

into equation of motion (2.11) gives

$$\ddot{a}_0 + s^2 \left(\frac{a}{h} + a_0 \right) = 0 \qquad (2.16)$$

$$\ddot{a}_n + [n^4 - n^2(1 + s^2) + s^2]a_n = s^2(n^2 - 1)\alpha_n \qquad (2.17)$$

A similar equation results for b_n. Pulse buckling modes have $n^2 \gg 1$, so Eq. (2.17) can be simplified to

$$\ddot{a}_n + s^2\eta^2(\eta^2 - 1)a_n = s^4\eta^2\alpha_n \qquad (2.18)$$

where $\eta = n/s$.

The solution to Eq. (2.18) with initial conditions $u(\theta, 0) = \dot{u}(\theta, 0) = 0$ is

$$a_n(\tau) = \frac{\alpha_n}{1 - \eta^2} \left[\begin{matrix} \cosh \\ \cos \end{matrix} \ p_n\tau \ - 1 \right] \qquad (2.19)$$

in which we have introduced a new dimensionless time τ and an argument parameter p_n defined by

$$\tau = s^2\hat{\tau}, \qquad p_n = \eta|1 - \eta^2|^{1/2} \qquad (2.20)$$

8

The cosh functions are taken for $\eta < 1$ and the cos functions for $\eta > 1$.

The function multiplying α_n in Eq. (2.19) is called the amplification function. Figure 2.1 gives an example of this function plotted against mode number n for $\tau = 6$ and mode number parameter $s = 20.67$. This value results for an aluminum 6061-T6 $(\sigma_y/E_t = 0.5)$ shell with radius-to-thickness ratio 8.4. This is a thicker shell than normally of interest, but the value of s is convenient for numerical results given later in the report.

An important feature of the amplification function is that at values of τ large enough for significant amplification, a band of modes are amplified with mode numbers ranging from somewhat below to somewhat above the value s. Neither very low nor very high order modes are amplified significantly. Also, the shape of the amplification function is independent of s, as can be seen from Eq. (2.19); amplification depends only on η and τ. Furthermore, even in thinner shells, which buckle during elastic or elastic-plastic radial motion, and for which the amplification function must be found by numerical integration, the resulting amplification function when plotted against a normalized wave number has essentially the same shape as that of the analytical result here.

These two properties of the amplification function have important implications for the work this report. The finite lower and upper mode number bounds and the universal shape, taken together, allow a convenient definition (in Chapter 3) of random imperfections that are proportional to an appropriate combination of wall thickness and buckle wavelengths. The universal shape allows Monte Carlo calculation of buckle waveform statistics that can be applied quite generally.

The relationship between white noise and equivalent single-mode imperfections can now be calculated quite generally from Eqs. (2.10) and (2.19). With $G(\eta,\tau)$ from Eq. (2.19), the G terms in Eq. (2.10) can be expressed as

$$\frac{1}{G_{\max}(\tau)}\left[\sum_{n=2}^{N} G^2(\eta,\tau)\right]^{1/2} = s^{1/2}R(\tau) \qquad (2.21)$$

where

$$R(\tau) = \frac{1}{G_{\max}(\tau)}\left[\int_{\eta_1}^{\eta_2} \frac{1}{1-\eta^2}\left(\begin{array}{c}\cosh \\ \cos\end{array} p(\eta,\tau) - 1\right)d\eta\right]^{1/2} \qquad (2.22)$$

in which we have used $d\eta = \Delta n/s = 1/s$ so that the sum can be replaced by an integral (s is typically large enough that η can be treated as a continuous

9

variable). Numerical integration of Eq. (2.22) shows that $R(\tau)$ depends weakly on τ. In the range $5 < \tau < 11$, $R(\tau)$ varies from 0.640 to 0.521. Since in this range G_{max} varies from 14 to 272, thresholds for buckling will certainly occur in this range. We therefore take $R = 0.60$ and the relationship between single-mode and random imperfections in Eq. (2.10) becomes

$$\sigma = \frac{\delta_n}{3s^{1/2}R(\tau)} = 0.556\,\delta_n s^{-1/2} \qquad (2.23)$$

Thus, the standard deviation of white noise imperfections to be used in finite element calculations decreases as $s^{-1/2}$ and hence as the inverse square root of the number of modes in the amplified range. This result occurs because we are adding each mode as a random variable and the deviation of the sum increases in a root-mean-square fashion. If we are to relate this deviation to experimental results based on equivalent single-mode imperfections, as indicated in Eq. (2.23), we must therefore know the bandwidth of the modes of buckling, which is part of the solution.

This bandwidth can be estimated on the basis of the same analytical solution used to obtain $G(\eta,\tau)$ in the above discussion. From the results given in Reference 2, pages 145 to 149, for representative aerospace metals at thresholds of pulse buckling, the material property parameter in the definition of s in Eqs. (2.13) is given by

$$\frac{\sigma}{E_t} = \left(\frac{8K}{3}\right)^{1/2}\frac{h}{a} \qquad (2.24)$$

In this more general theory, instantaneous stress σ rather than yield stress σ_y is used, and both σ and E_t are assumed to vary with compressive strain according to a stress-stain relationship characterized by the yield strain and a shape factor K. The right hand side of Eq. (2.24) gives the value of the material property ratio at the final compressive hoop strain imparted by the critical impulse for buckling, which depends on the radius-to-thickness ratio of the shell as given in the formula. Substitution of Eq. (2.24) into Eq. (2.13) gives

$$s^2 = 12\left(\frac{8K}{3}\right)^{1/2}\frac{h}{a}\frac{a^2}{h^2} = (384\,K)^{1/2}\frac{a}{h} \qquad (2.25)$$

With this value for s, Eq. (2.23) becomes

$$\sigma = 0.264\,K^{1/8}\left(\frac{a}{h}\right)^{-1/4}\delta_n \qquad (2.26)$$

10

In Reference 2, equivalent single-mode imperfections of $\delta_n = 0.01\,h$ are shown to give reasonable agreement between experiment and theory for critical impulses at thresholds of observable buckles. The corresponding standard deviation of white noise imperfections from Eq. (2.26) for $K = 15$ (an appropriate value for hardened alloys of aluminum, titanium and magnesium) and $a/h = 100$ is $0.00060\,h$.

For finite element calculations, the magnitude of imperfections to correlate theory and experiment are expected to be larger than this value because of neglect in the analytical theory of the decrease in hoop thrust with increasing buckle growth. Thus, near and beyond the threshold of significant buckling, in the analytical theory the buckle amplitudes grow unrealistically with increasing time and hence increasing impulse.

11
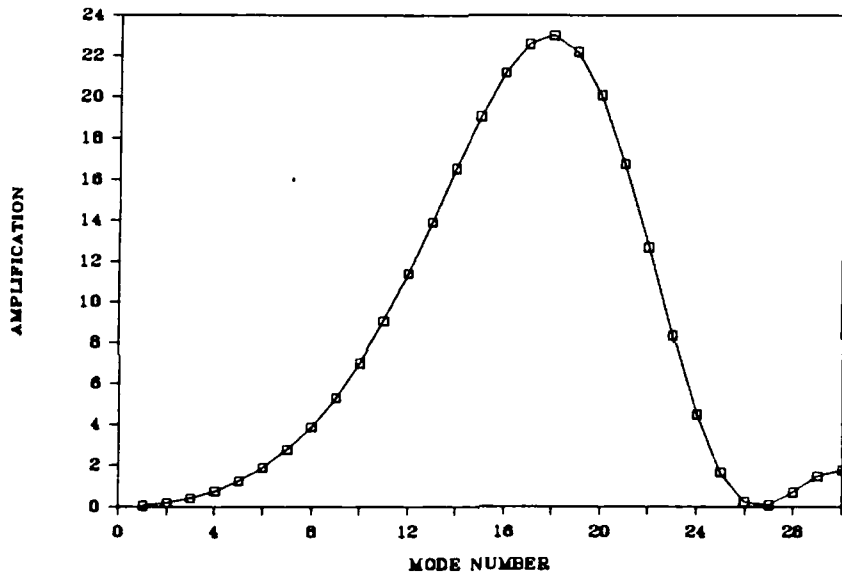
Figure 2.1: Amplification function, $s = 20.67$, $\tau = 6$.

12

Section 3

Random Imperfections
Proportional to Wall
Thickness and Buckle
Wavelengths

The white noise imperfections discussed in the previous chapter are physically unsatisfying because the resulting Fourier series for the imperfections does not converge. It was nevertheless possible to use this form because the finite bandwidth of the series for the buckle shapes gave truncated and hence bounded series for buckle shapes. However, this puts a premium on specification of the bounding mode number N to be used in calculating response with finite element methods. If N is made conservatively large, the imperfections have large amplitude components at short wavelengths that may be difficult to treat numerically even though they are eventually suppressed in comparison with the dominant shape of the buckled form, which grows with time.

It is therefore useful to explore other forms of random imperfections that are better behaved and are based on expectations for imperfections to be found in actual shells. One such form is explored in this chapter. Other forms may be appropriate for specific applications in which information is available about the manufacturing processes that introduce imperfections.

ın the remainder of this chapter we first give example imperfection shapes to demonstrate the difficulty with white noise imperfections dis-

cussed above. Then we describe the proposed alternative form of random imperfections and show how this form relates to single-mode imperfections. Example imperfection shapes with this form are compared with the white noise shapes for the same set of random numbers. Then the buckle shapes that result from these imperfections are given at a sequence of increasing times, to show how the buckling process greatly modifies the imperfection shape and increases its amplitude.

3.1   White Noise Imperfection Shapes

Figures 3.1 through 3.7 give imperfection shapes calculated with Eq. (2.1) for random coefficients α_n and β_n having a Gaussian distribution and a constant standard deviation of unity. In each figure, the series is truncated at N, with N ranging from 5 in Figure 3.1 to 60 in Figure 3.7.

If we assume that buckling is to be investigated for a problem having the amplification function in Figure 2.1, then the modes of most concern range from about 10 to somewhat less than 30. However, in a finite element calculation we have little apriori knowledge of this function except that its general shape will be similar to that in Figure 2.1. We would therefore have to take N conservatively large to ensure that the significantly amplified components are included in the calculation.

Without extensive experience, it is unlikely that one would know the dominant wavelengths to within a factor of two, so even a value of $N = 60$ would not be too conservative in a calculation for which the amplification function turns out to have the amplified band given in Figure 2.1. Comparison of the white noise imperfection shapes in Figures 3.4 and 3.7 for $N = 30$ and $N = 60$, respectively, shows a substantial difference in both shape and amplitude. With $N = 30$, few peaks have amplitudes larger than 10, while with $N = 60$ there are many peaks with amplitudes near 20. Also, the wavelengths associated with these peaks are about a factor of 2 shorter than with $N = 30$.

Thus, while the buckle motion will not amplify these short wavelengths, they tend to dominate the imperfection shape and hence require accuracy in the calculation at these wavelengths. The imperfection form described in the following paragraphs relieves this accuracy requirement while better representing physically expected forms of imperfections.

14

3.2 Adaptation of Imperfection Formula from Static Buckling

Near the turn of the century, hundreds of experiments were performed on static axial buckling of columns to determine values of imperfections to be used in design. The approach in those experiments was the same as that used in Reference 2 for dynamic pulse buckling, namely that, because the imperfections were too small and diverse to measure, equivalent imperfections were calculated on the basis of observed buckling deformations interpreted with the theory to be used in design analysis.

Although the imperfections scattered widely, the general trend suggested use of the following formula in column design:

$$a_1 = 0.1 \frac{r^2}{c} + \frac{L}{250} = \frac{1}{60}\left(h + \frac{L}{12.5}\right) \tag{3.1}$$

in which a_1 is the coefficient of an equivalent imperfection in the half sinewave shape $\sin \pi x/L$ of the Euler column of length L, r is the radius of gyration of the cross section and c is the distance from the neutral axis to an extreme fiber. This is Eq. (2.2.24) from Reference 2. In the second expression the formula is applied for the specific case of a rectangular column of depth h.

The essential observation used in suggesting Eq. (3.1) was that column imperfections are expected to have two components, one proportional to its depth and the other proportional to its length. It is reasonable to take a similar approach for pulse buckling of shells. In this case, the length is the half wavelength of each buckling mode. We therefore take the standard deviation of the random imperfection coefficients in the form

$$\sigma = C\left(h + \frac{L_n}{12.5}\right) = Ch\left(1 + \frac{\pi a}{12.5\,n}\right) = Ch\left(1 + \frac{a}{4hn}\right) \tag{3.2}$$

While this form is more physically reasonable than pure white noise, in that the coefficients become smaller at shorter wavelengths, the constant term, proportional to shell thickness, gives a component that is white noise and hence gives a Fourier series for the imperfections that does not converge. It is therefore useful to replace this expression by a function that converges while giving approximately the same values for σ as from Eq. (3.2) over the bandwidth of concern for pulse buckling.

15

One such function is

$$\sigma = Bhn^{-1/2} \tag{3.3}$$

This is a convenient form that matches the values from Eq. (3.2) to within 20% and more frequently within 10% for all shells of interest. A good match is obtained because the exponent $-1/2$ is midway between the exponents 0 and -1 in Eq. (3.2). Also, this exponent is the separator between imperfections series that do and do not converge; an expression analogous to Eq. (2.4) shows that the terms for the variance of the imperfection shape decrease as $1/n$, which is the harmonic series.

An exact match between Eqs. (3.2) and (3.3) is forced at the peak of the amplification function, which gives

$$B = Cn_{cr}^{1/2}\left(1 + \frac{a}{4hn_{cr}}\right) \tag{3.4}$$

where n_{cr} is the mode number of the most amplified mode, which from Eq. (2.25) is given by

$$n_{cr} = \frac{s}{\sqrt{2}} = (96\,K)^{1/4}\left(\frac{a}{h}\right)^{1/2} \approx 6\left(\frac{a}{h}\right)^{1/2} \tag{3.5}$$

In the last expression we have taken $K = 15$, for which $(96\,K)^{1/4} = 6.16$.

With this value for n_{cr}, substitution of Eq. (3.4) into Eq. (3.3) yields the desired expression for imperfection deviations:

$$\sigma = C\sqrt{6}\left(\frac{a}{h}\right)^{1/4}\left[1 + \frac{1}{24}\left(\frac{a}{h}\right)^{1/2}\right]hn^{-1/2} \tag{3.6}$$

Over the bandwith of significantly amplified modes, from $0.5\,n_{cr}$ to $1.5\,n_{cr}$, see Figure 2.1, deviations from Eq. (3.6) match those from Eq. (3.2) to within 10% for $a/h > 100$. The match improves with increasing a/h. At $a/h = 10$, the thickest shell of interest, the match is within 20%. These accuracies are far better than our knowledge of imperfection amplidudes, so Eqs. (3.2) and (3.6) are essentially equivalent.

16

3.3 Relationship with Single-Mode Imperfections

With σ now varying with n as given by Eq. (3.6), Eq. (2.4) for $\overline{u^2}(\tau)$ becomes

$$\overline{u^2}(\tau) = A^2 \sum_{n=2}^{N} \frac{1}{n} G^2(n,\tau) \tag{3.7}$$

where

$$A = C\sqrt{6} \left(\frac{a}{h}\right)^{1/4} \left[1 + \frac{1}{24}\left(\frac{a}{h}\right)^{1/2}\right] h \tag{3.8}$$

Substitution of $n = \eta s$ and $d\eta = 1/s$ into Eq. (3.7) gives

$$\overline{u^2}(\tau) = A^2 \int_{\eta_1}^{\eta_2} \eta^{-1} G^2(\eta,\tau)\, d\eta \tag{3.9}$$

If we relate single-mode and random imperfections by setting three times the root-mean-square buckle deformation equal to the peak deformation with a single-mode imperfection, as was done for Eq. (2.10), we obtain

$$3A \left[\int_{\eta_1}^{\eta_2} \eta^{-1} G^2(\eta,\tau)\, d\eta\right] = \delta_n G_{\max} \tag{3.10}$$

from which

$$A = \frac{\delta_n}{3} \cdot \frac{1}{R_1(\tau)} \tag{3.11}$$

where

$$R_1(\tau) = \frac{1}{G_{\max}(\tau)} \left[\int_{\eta_1}^{\eta_2} \eta^{-1} G^2(\eta,\tau)\, d\eta\right]^{1/2} \tag{3.12}$$

Integration to find $R_1(\tau)$ gave values from 0.705 to 0.605 for τ in the range of interest from 5 to 11. The small change in R_1 reflects the nearly constant shape of the amplification function in this range. If we take $R_1 = 0.65$, then

$$A = \frac{\delta_n}{3(0.65)} = 0.51\, \delta_n \tag{3.13}$$

The expression depending on a/h in the definition of A in Eq. (3.8) evaluates to values from 2.51 to 4.48 for a/h in the range 20 to 100 where most of

17

the experiments reported in Reference 2 were performed. We take a value of 3 to solve for C from Eqs. (3.8) and (3.13), which gives

$$C\sqrt{6} = \frac{0.51\,\delta_n}{3h} = 0.17\,\frac{\delta_n}{h} \qquad (3.14)$$

Assuming $\delta_n = 0.01\,h$, as was done in Chapter 2, substitution of Eq. (3.14) into Eq. (3.6) results in the following expression for the standard deviations of random imperfections:

$$\sigma = 0.0017\left(\frac{a}{h}\right)^{1/4}\left[1 + \frac{1}{24}\left(\frac{a}{h}\right)^{1/2}\right]hn^{-1/2} \qquad (3.15)$$

When used in the analytical theory in Reference 2, these deviation magnitudes will result in random buckle shapes comparable in magnitude to those for single-mode imperfections. However, as pointed out in Chapter 2 for white noise imperfections, the magnitude of imperfections to be used in finite element calculations are probably larger than these from the analytical theory because of neglect in the analytical theory of hoop thrust reduction as the buckles grow.

3.4 Example Imperfection and Buckle Shapes

The improved behavior of random imperfection shapes with Fourier coefficients proportional to $n^{-1/2}$ is demonstrated in Figures 3.8 through 3.14. These were calculated with Eq. (2.1) using coefficients from Eq. (3.3) with $Bh = 1$ and the same set of 120 random coefficients used to calculate the truncated white noise imperfection shapes given in Figures 3.1 through 3.7. The truncation numbers N are also the same in both sets of figures, so the sets can be compared figure by figure.

The first observation is that, with a $n^{-1/2}$ variation in standard deviation, peak amplitudes change only from about 3.5 with $N = 5$ (Figure 3.8) to 7 with $N = 60$ (Figure 3.14). In fact, all but two peaks with $N = 60$ are less than 4.5. The same comparison for white noise imperfections shows an increase in peak amplitudes from 5 with $N = 5$ (Figure 3.1) to more than 20 with $N = 60$ (Figure 3.7).

Also, since this change in amplitude is from higher mode numbers, with white noise coefficients the shape with $N = 60$ is dominated by short wavelengths while with $n^{-1/2}$ coefficients the character of the longer wavelengths

18

remains dominant with $N = 60$. Thus, the longer wavelength features with $N = 30$ (Figure 3.11) are still apparent with $N = 60$ (Figure 3.14). In a similar comparison for white noise, the long wavelength features with $N = 30$ (Figure 3.4) are barely detectable with $N = 60$ (Figure 3.7). Other comparisons can be made for other trunctation modes with the same result.

It is also instructive to observe how the initial imperfection shape transforms into a buckled shape under the influence of pulse buckling amplification. Figures 3.15 through 3.20 give a series of snapshots of buckle shapes at dimensionless times from $\tau = 0$ through 10. These were calculated with the imperfection shape in Figure 3.14 using an amplification function given by Eq. (2.19). The vertical scale is the same in all the plots except for the last plot at $\tau = 10$, at which the amplification is larger than generally of interest. The plot at $\tau = 0$ is of the itentical imperfection shape as in Figure 3.14 except for the scale change.

The quantity plotted is the 'total' buckle shape, consisting of the sum of the imperfection and the buckle deformation. This is done to illustrate that by $\tau = 6$ there is no evidence of the imperfection shape in the total buckle shape even though the maximum peak has increased by only a factor of 7. It also shows graphically how the short wavelength features essentially disappear with increasing time. At $\tau = 2$ and 4, there is much short wavelength activity. By $\tau = 6$ this activity has ceased and a dominant buckle form has been established.

Beyond $\tau = 6$ the main change with time is simply an increase in the amplitude of this established shape. This occurs even though the theory is linear. In a finite element calculation, which will include plastic yielding in the form of hinges at the buckle peaks, the wavelengths also become fixed as time increases. Thus, this simple theory contains many of the features of a more complete analysis.
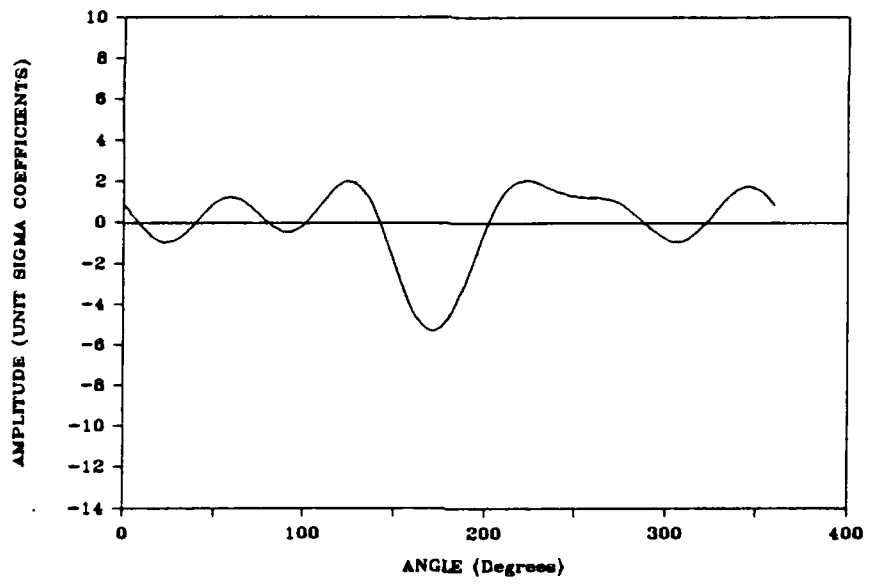
Figure 3.1: Truncated white noise imperfection shape, $N = 5$.
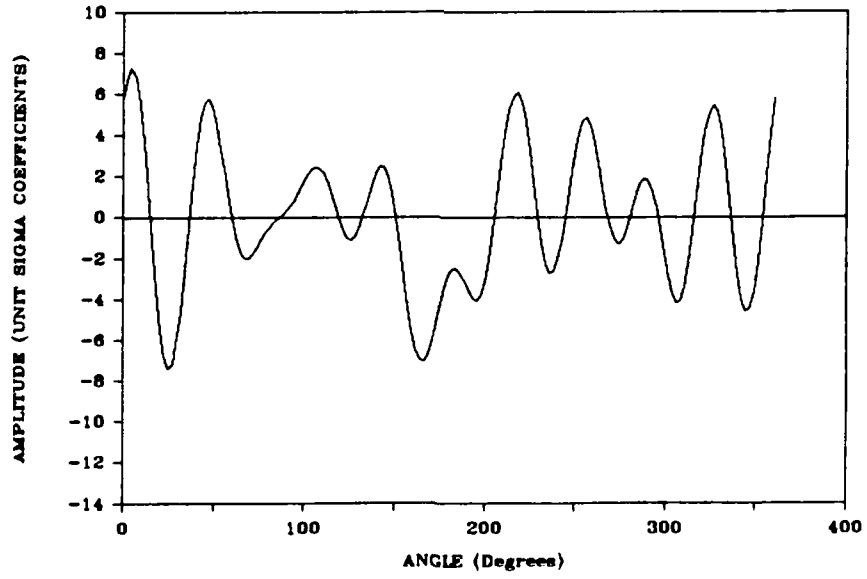
Figure 3.2: Truncated white-noise imperfection shape, $N = 10$.

20
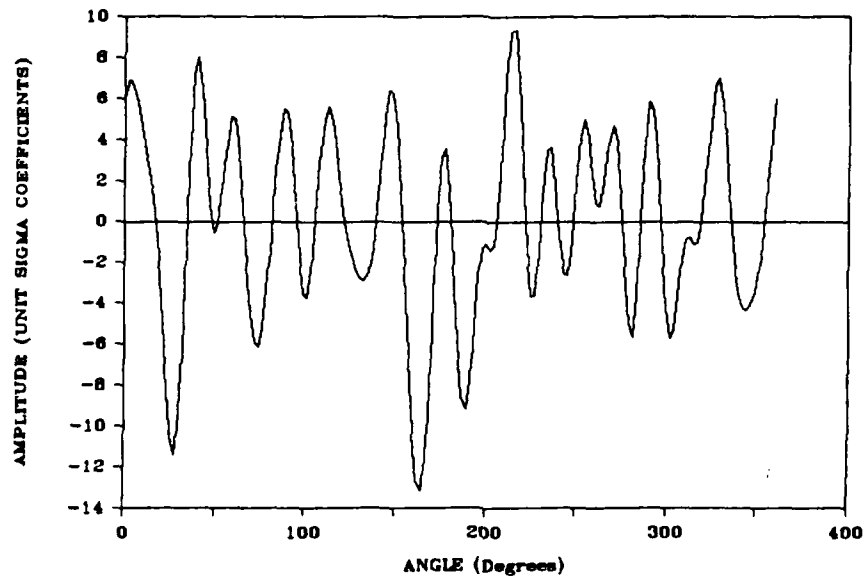
Figure 3.3: Truncated white-noise imperfection shape, $N = 20$.
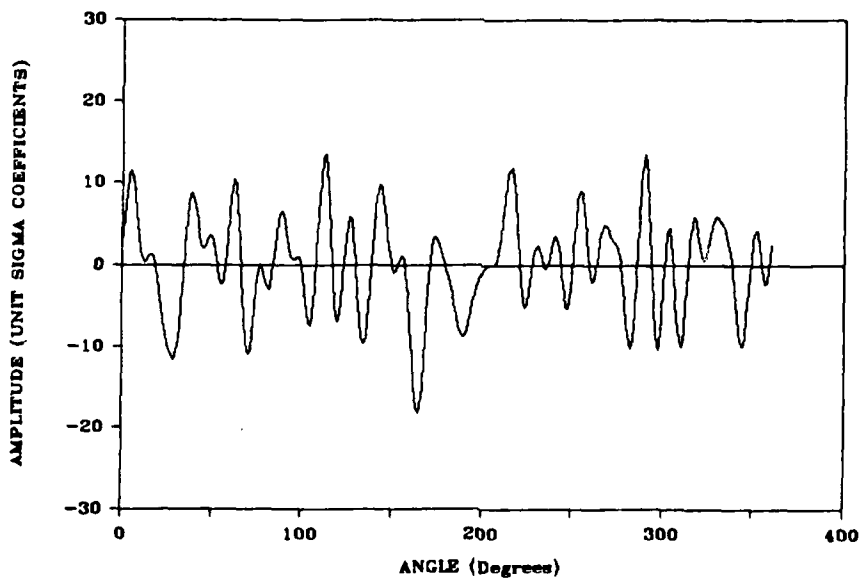
Figure 3.4: Truncated white-noise imperfection shape, $N = 30$.

21
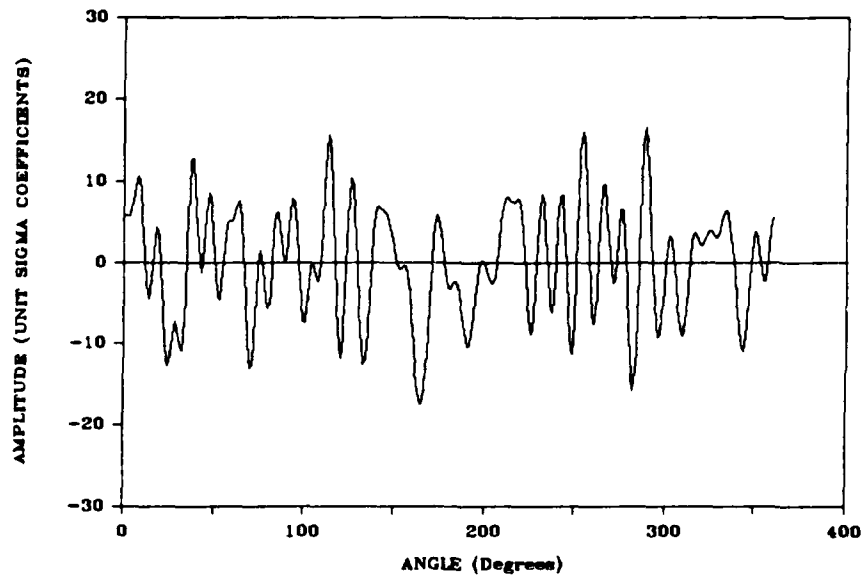
Figure 3.5: Truncated white-noise imperfection shape, $N = 40$.
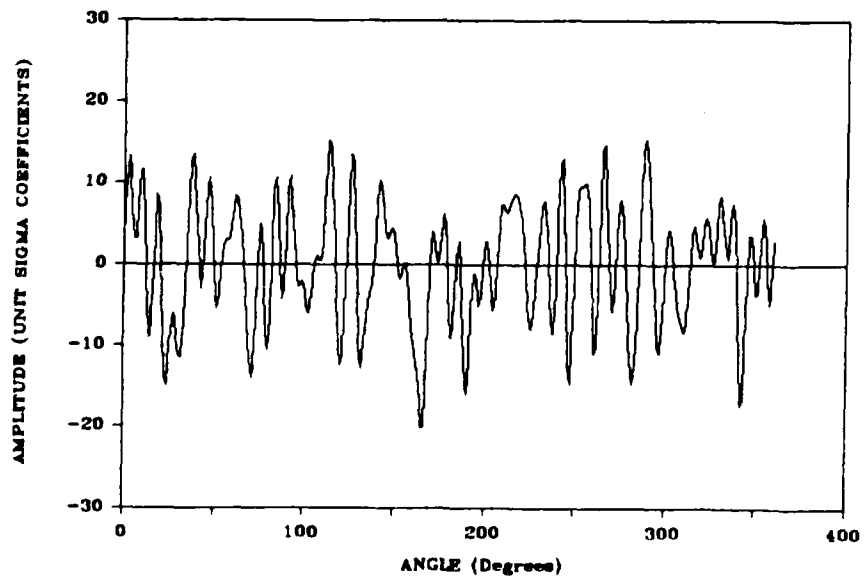
Figure 3.6: Truncated white-noise imperfection shape, $N = 50$.

22
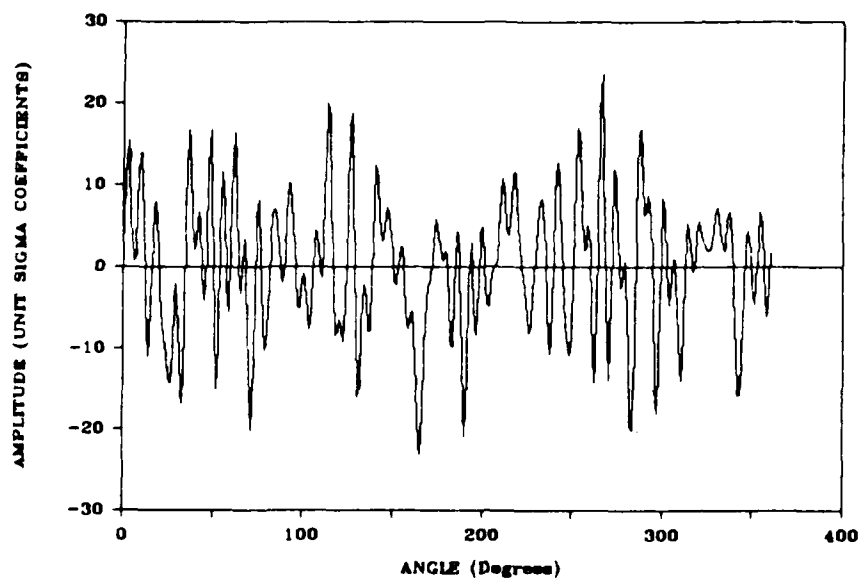
Figure 3.7: Truncated white-noise imperfection shape, $N = 60$.
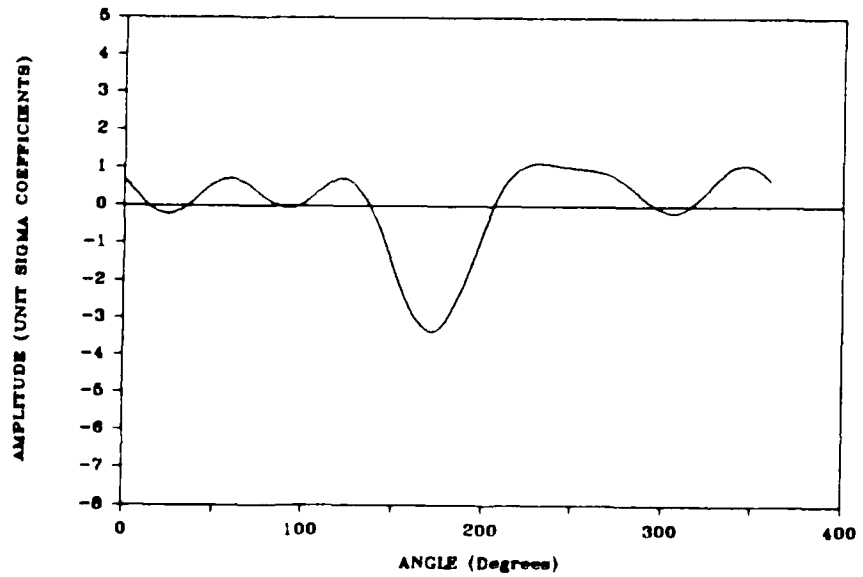
Figure 3.8: Random imperfection, $n^{-1/2}$ coefficients, $N = 5$.

23
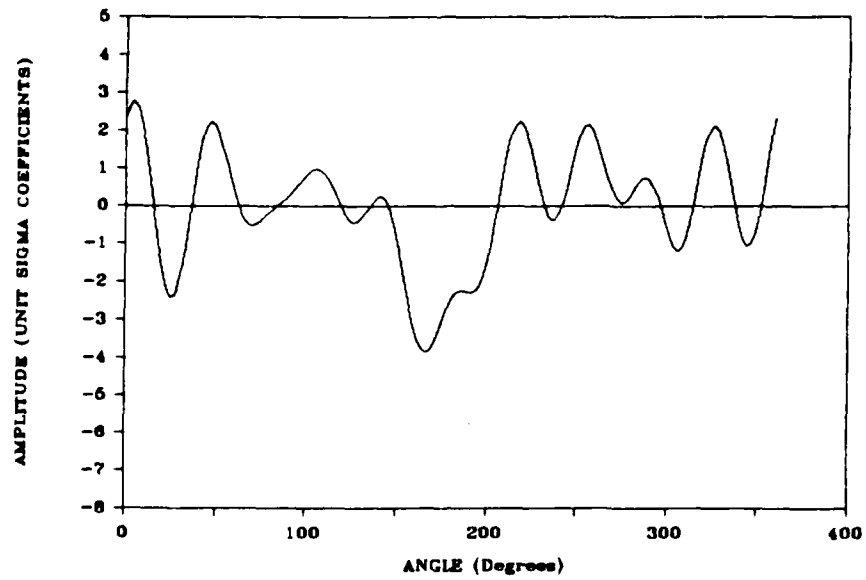
Figure 3.9: Random imperfection, $n^{-1/2}$ coefficients, $N = 10$.
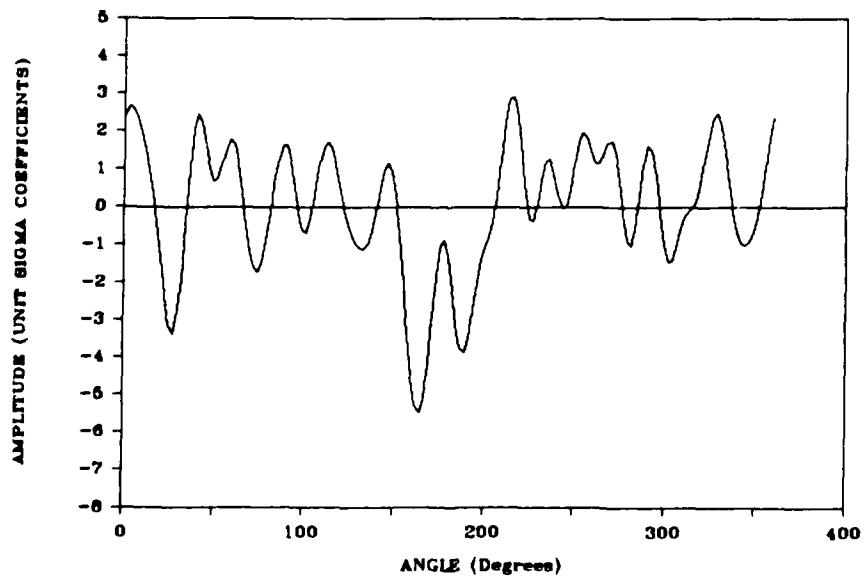
Figure 3.10: Random imperfection, $n^{-1/2}$ coefficients, $N = 20$.

24
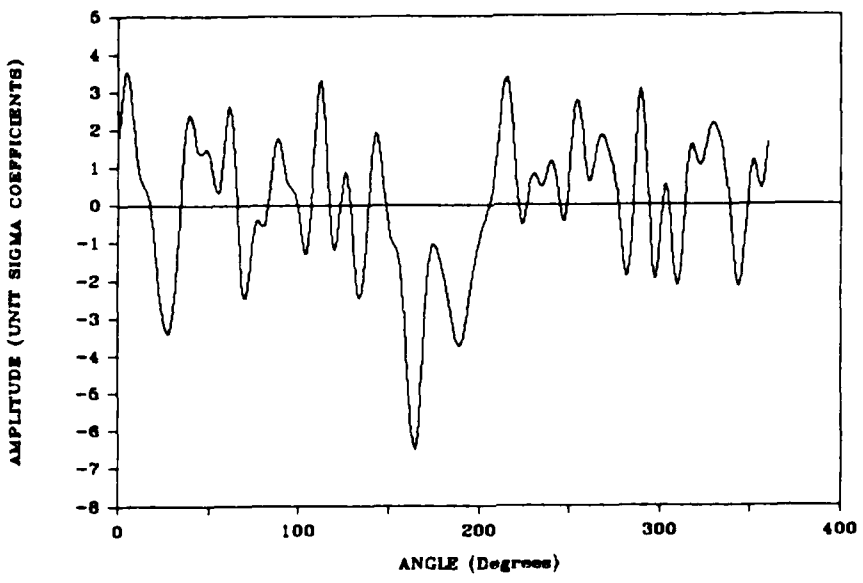
Figure 3.11: Random imperfection, $n^{-1/2}$ coefficients, $N = 30$.
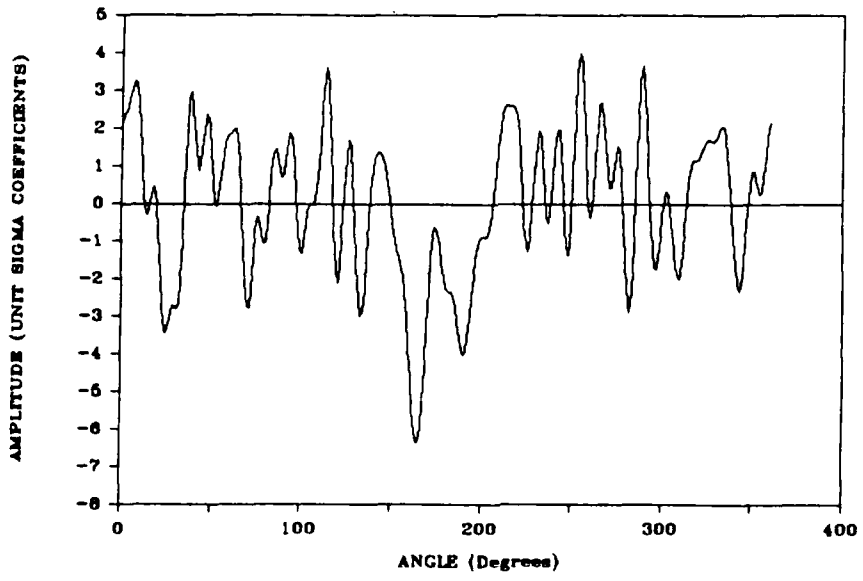
Figure 3.12: Random imperfection, $n^{-1/2}$ coefficients, $N = 40$.

25
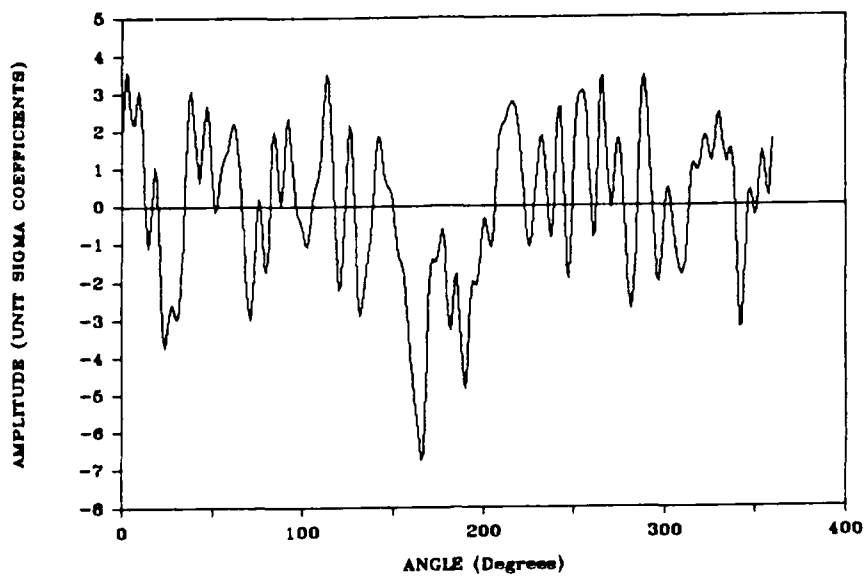
Figure 3.13: Random imperfection, $n^{-1/2}$ coefficients, $N = 50$.
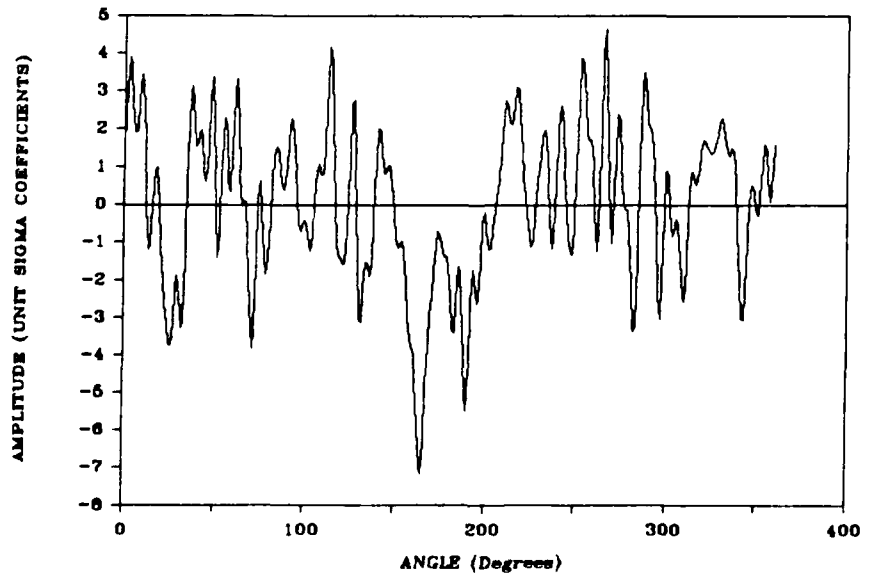
Figure 3.14: Random imperfection, $n^{-1/2}$ coefficients, $N = 60$.

26
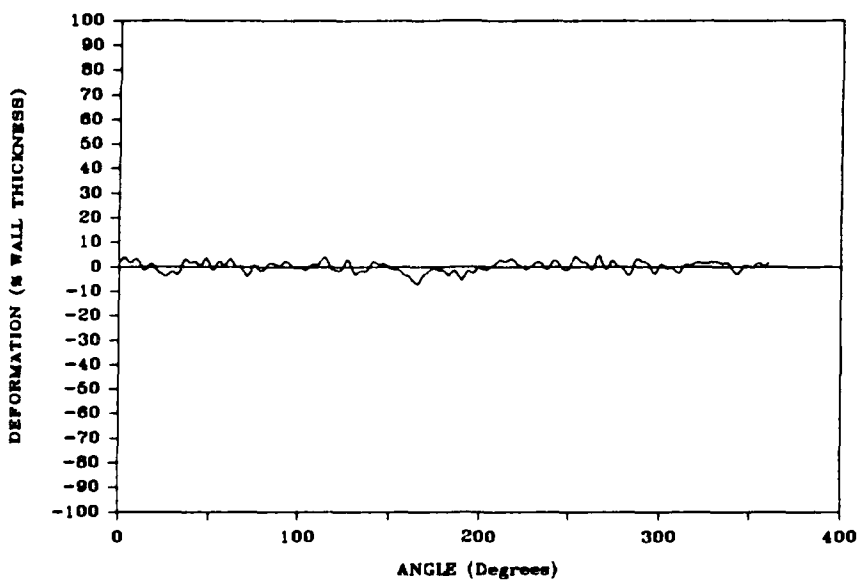
Figure 3.15: Buckle shape from random imperfection, $\tau = 0$.
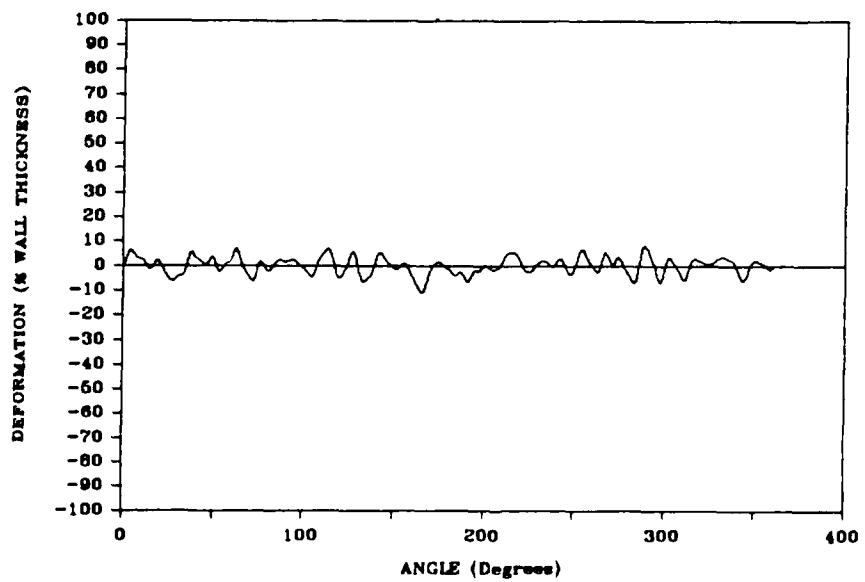
Figure 3.16: Buckle shape from random imperfection, $\tau = 2$.

27
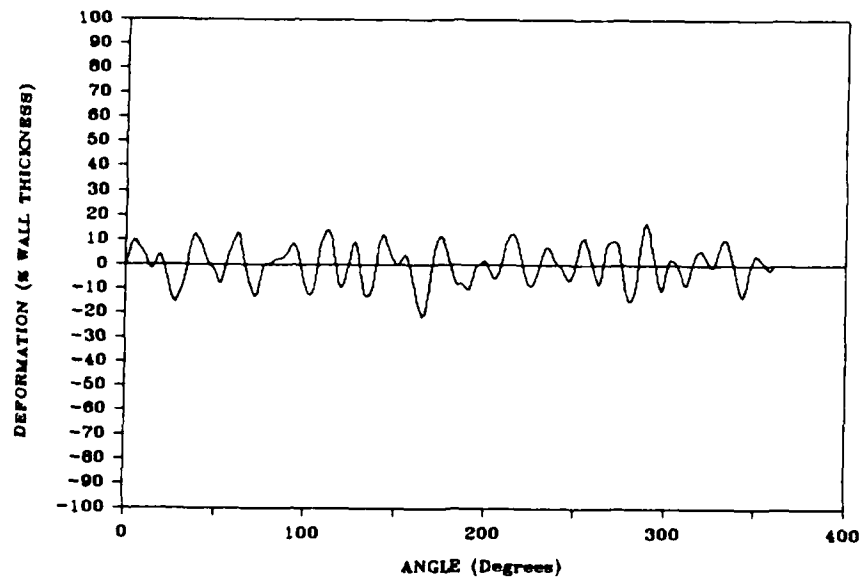
Figure 3.17: Buckle shape from random imperfection, $\tau = 4$.
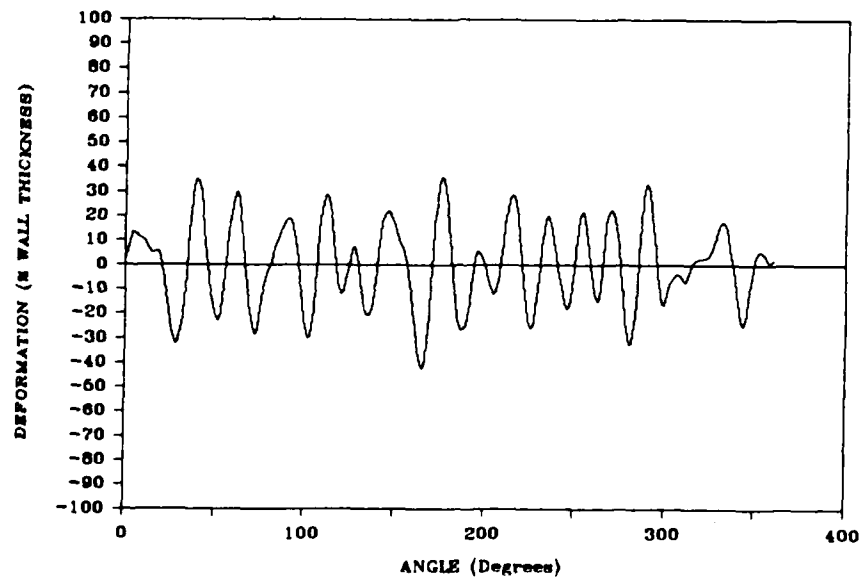
Figure 3.18: Buckle shape from random imperfection, $\tau = 6$.

28
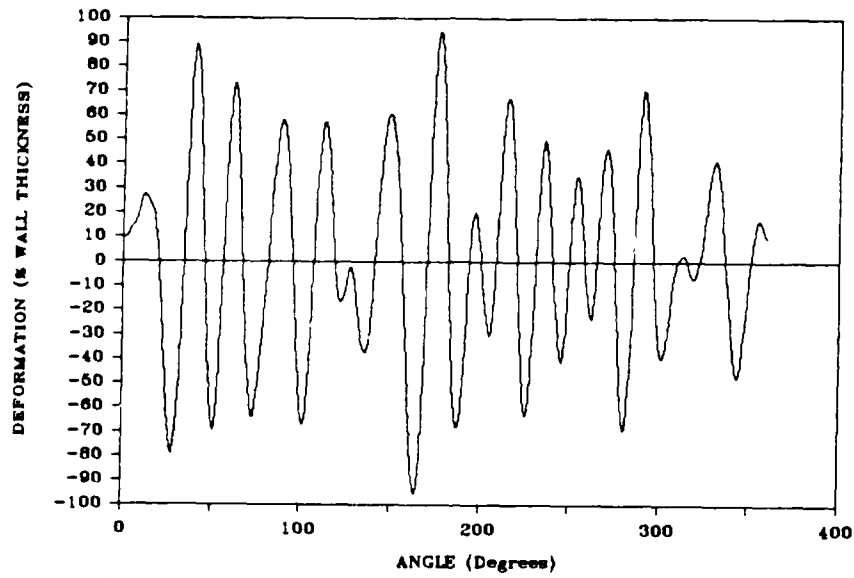
Figure 3.19: Buckle shape from random imperfection, $\tau = 8$.
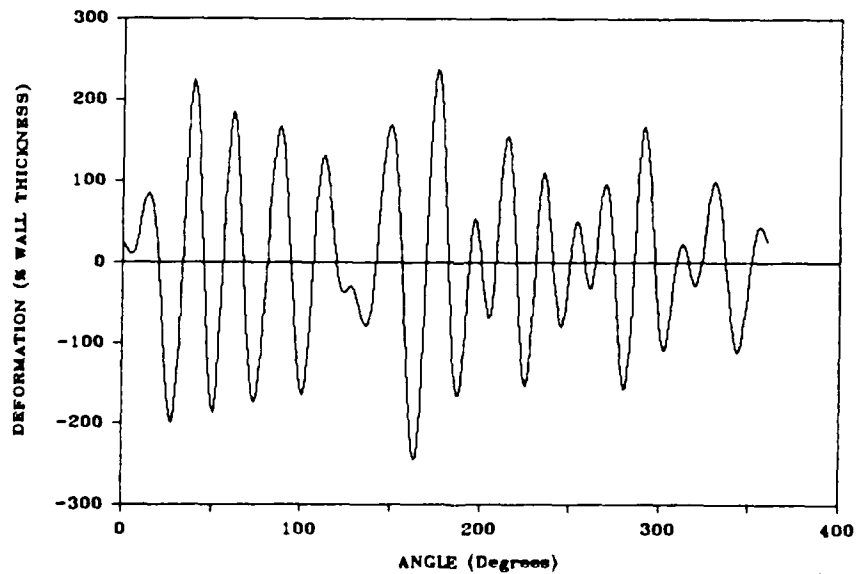
Figure 3.20: Buckle shape from random imperfection, $\tau = 10$.

29

Section 4

Statistics of Buckle Shapes

With imperfections in random form, the resulting buckle shapes are also random and must be described statistically. The mathematical transformation from imperfections to buckle shapes is too complex to allow analytical formulation of buckle statistics even for the simple buckling theory summarized in Chapter 2. The single exception is the mean wavelength, for which an explicit formula is given in Reference 2 based on a derivation in Reference 3. More general statistics are therefore calculated in this chapter by the Monte Carlo method.

The same situation is true for finite element calculations except that Monte Carlo calculations would be much more time consuming and expensive. We therefore also investigate in this chapter how the statistics of buckle shapes from single buckle calculations can be used to estimate the statistics of the universe of buckle shapes. The statistics examined are the means and standard deviations of the wavelengths and peak-to-peak amplitudes of the buckle shapes.

4.1   Random Number Generator

The random number generator used for these calculations is the function *RND* in MS BASIC running on an IBM PC. This function returns random numbers uniformly distributed in the interval 0, 1. Thus, a function x, with mean value zero and uniformly distributed in the interval $-1/2$, $1/2$ is given by

$$x = RND - 1/2 \qquad (4.1)$$

The standard deviation of x is found from

$$\sigma_x^2 = \int_{-1/2}^{1/2} x^2 p(x)\, dx = \frac{1}{12} \tag{4.2}$$

where the probability density function $p(x) = 1$ for the unit interval.

From the central limit theorem, random numbers with a Gaussian distribution are obtained by adding M values of x.

$$y = \sum_{i=1}^{M} x_i = \sum_{i=1}^{M} RND - \frac{M}{2} \tag{4.3}$$

The standard deviation of M independent random variables is

$$\sigma_y^2 = M\sigma_x^2 \tag{4.4}$$

The desired random numbers with zero mean value and unit standard deviation are therefore obtained with

$$z = \left(\sum_{i=1}^{M} RND - \frac{M}{2} \right) \left(\frac{12}{M} \right)^{1/2}. \tag{4.5}$$

Several tests were run to demonstrate the uniformity of the $R\dot{N}D$ function. Results from one such test are given in Figure 4.1, which is a screen dump from a raster size of 200 × 640. Each point in the scatter diagram was obtained by two calls to RND, one of which was multiplied by the screen width and the other by the screen height. The points are uniformly distributed over the screen, as desired, and were uniformly distributed throughout the calculation as the screen filled with points.

The Gaussian distribution function in Eq. (4.5) was checked for $M = 10$ by creating a histogram from 1000 calls to the function. The resulting histogram is given in Figure 4.2. The diagram is biased a half bar width to the right because of the graphics generation method. The distrubution is a good approximation to a Gaussian distribution.

4.2   Statistics of the Universe of Buckle Shapes

Population statistics of a universe of buckle shapes were approximated by calculating 16 buckle shapes with the amplification function in Figure 2.1

[Eq. (2.19) with s = 20.67]. In these calculations, and all the calculations in this report, a Gaussian parameter value $M = 10$ was used in Eq. (4.5). Imperfections for this statistical study were taken in white noise form with Fourier coefficients having unit standard deviation. This was done so as not to specialize to any particular variation of Fourier coefficients with mode number n. Although use of the $n^{-1/2}$ variation suggested in this report looks promising, other forms may be proposed in the future based on knowledge or measurements of imperfections for particular manufacturing methods.

The resulting shapes are given in Figures 4.3 through 4.18. The entire sequence is given because it is useful to scan through the figures to see the range of buckle shapes that are members of the same population. Some of the shapes are fairly regular, and one can easily imagine approximating the shape with a single buckle mode, as in Figure 4.7, for example. Others are quite irregular and deviate substantially from a single-mode representation, as in Figure 4.15. The most frequently occuring buckle shape has buckles at nearly constant wavelength beating against modes of nearby wavelengths, resulting in an undulating amplitude. This is most clearly demonstrated by Figure 4.6. The beat wavelength depends on the separation between groups of mode numbers that happen to have large imperfection coefficients.

The statistics of peak-to-peak amplitudes were obtained by calculating negative-to-positive and positive-to-negative amplitude differences of all the peaks in the 16 buckle shapes. A histogram of the resulting values is given in Figure 4.19. The histogram is sufficiently filled in that it is taken to represent the distribution of the universe of buckle shapes. It has a fairly well-defined maximum probability near 140 units of magnitude and a finite probability at zero magnitude, reflecting the many small wiggles seen in Figures 4.3 through 4.18. The average amplitude is 152 units and the standard deviation is 83 units.

4.3   Estimates of Buckle Wave Population Statistics

The isolated vertical tic marks labeled 152 and +83 at the top of Figure 4.19 are drawn at the average amplitude and at one standard deviation above and below the average. The bars drawn just below the 152 and +83 tic marks give the range of average values and standard deviations calculated

32

for the individual buckle shapes, as given on the plots in Figures 4.3 through 4.18. These demonstrate that statistics calculated from buckle waves in a single buckling calculation give reasonably good estimates for the statistics of the universe of buckle waves. Thus, in finite element analysis, it appears that one or two calculations should give good estimates for buckle statistics.

Figure 4.20 gives the distribution of wavelengths for the collection of 16 buckle shapes. The distribution has a pronounced maximum near 19 degrees. Nearly all the wavelengths lie between 10 and 30 degrees. An explicit formula for the mean wavelength as a function of time is given in Reference 2.
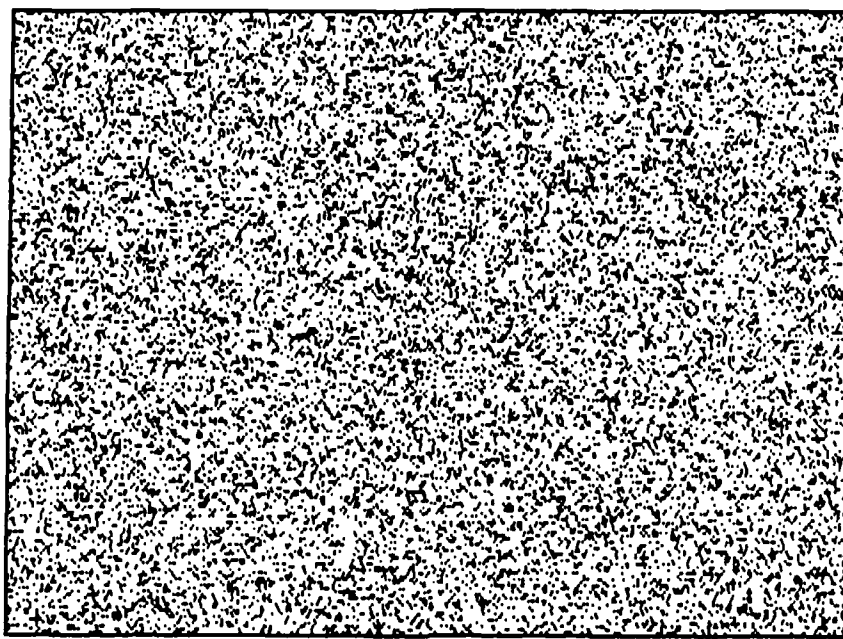
Figure 4.1: Scatter diagram for *RND* numbers, 640 × 200 raster.
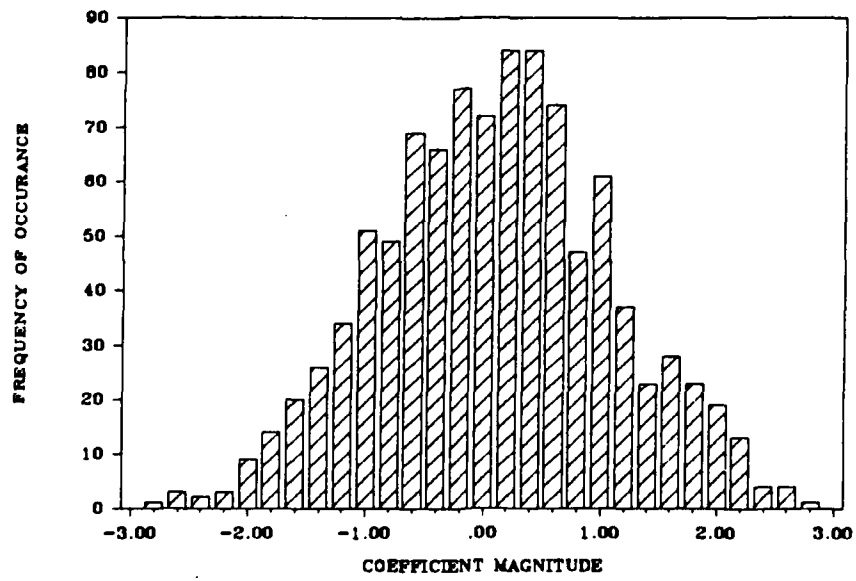
Figure 4.2: Histogram test of *RND* Gaussian coefficient generator.

34
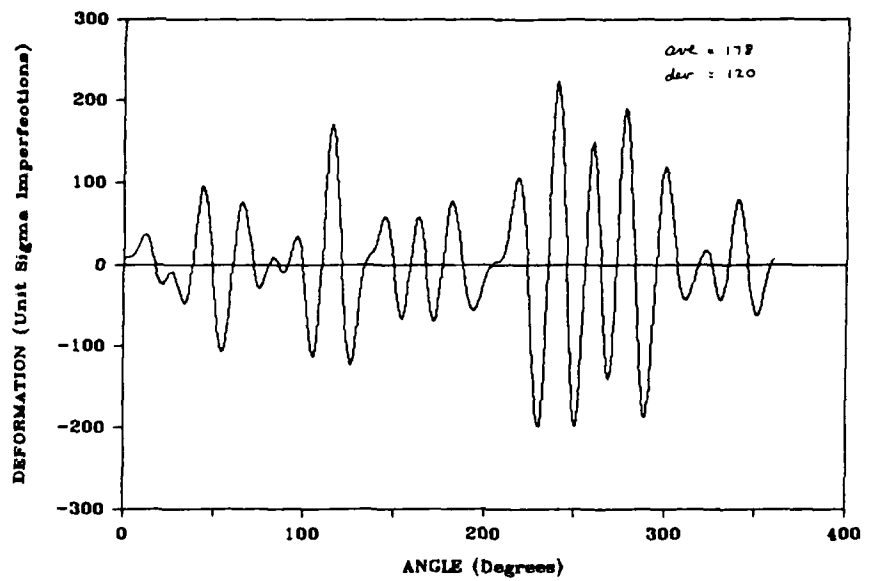
Figure 4.3: Buckle shape from white-noise imperfections, $s = 20.67$, $\tau = 6$, case 1.
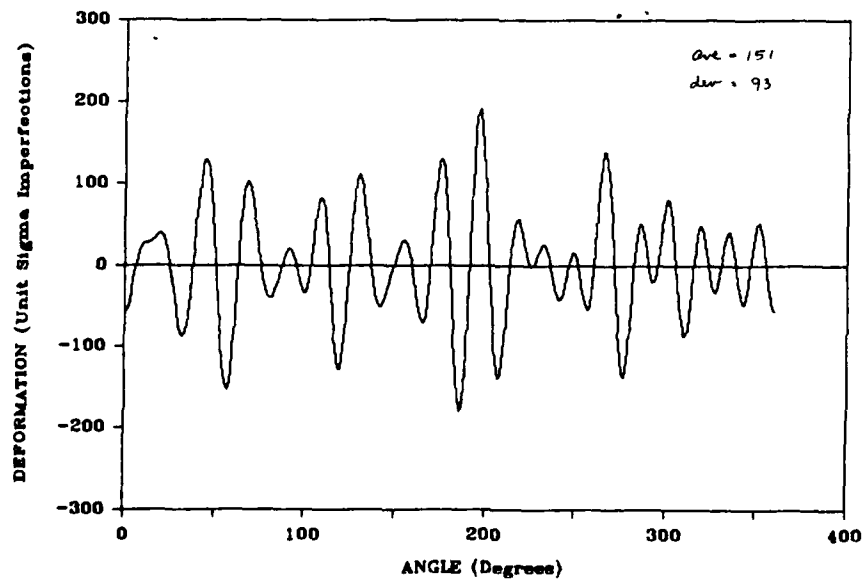
Figure 4.4: Buckle shape from white-noise imperfections, $s = 20.67$, $\tau = 6$, case 2.

35
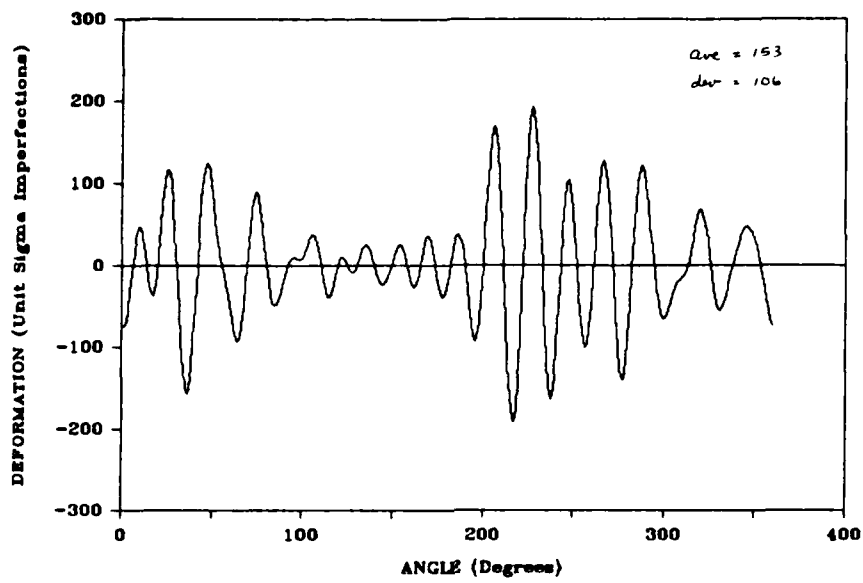
Figure 4.5: Buckle shape from white-noise imperfections, $s = 20.67$, $\tau = 6$, case 3.
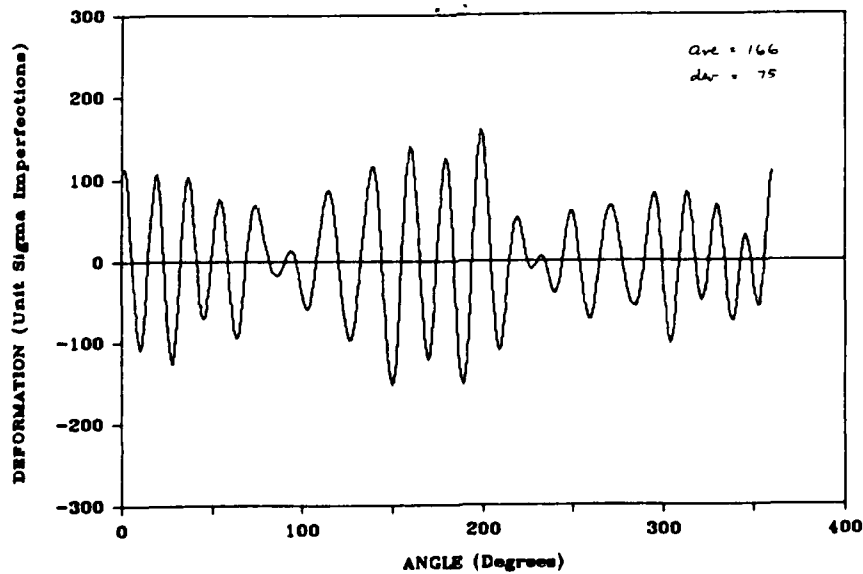
Figure 4.6: Buckle shape from white-noise imperfections, $s = 20.67$, $\tau = 6$, case 4.

36
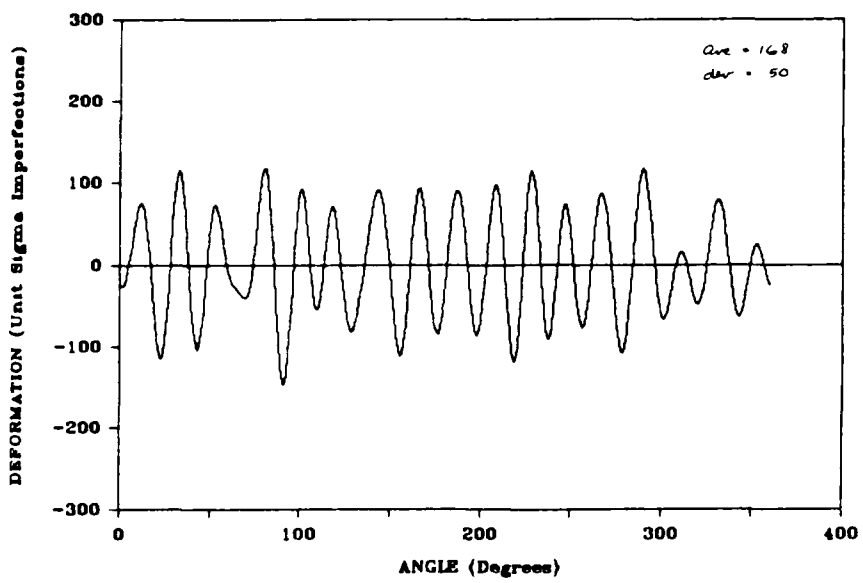
Figure 4.7: Buckle shape from white-noise imperfections, $s = 20.67$, $\tau = 6$, case 5.
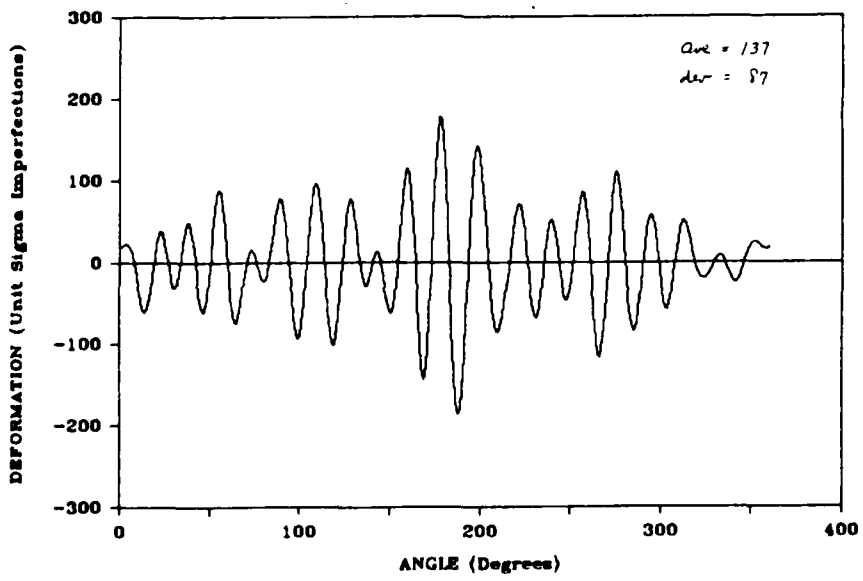
Figure 4.8: Buckle shape from white-noise imperfections, $s = 20.67$, $\tau = 6$, case 6.
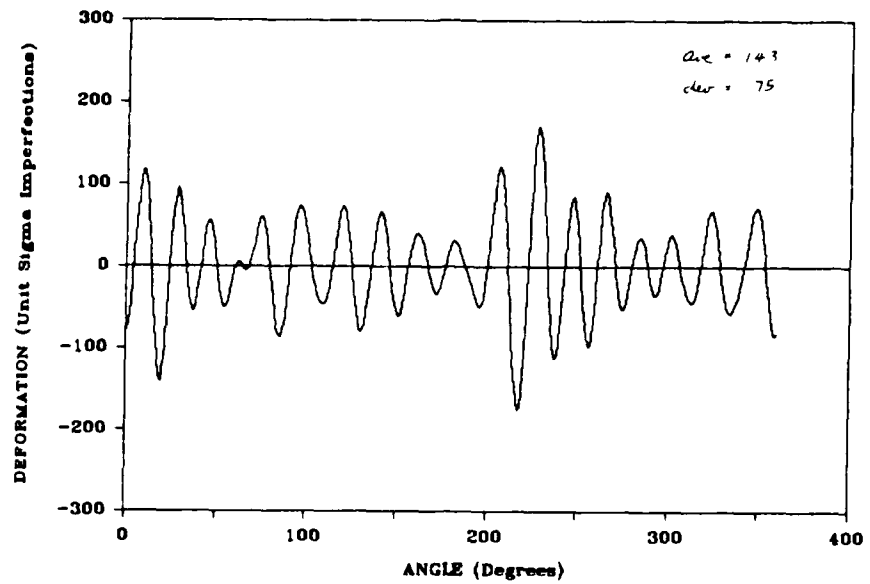
Figure 4.9: Buckle shape from white-noise imperfections, $s = 20.67$, $\tau = 6$, case 7.
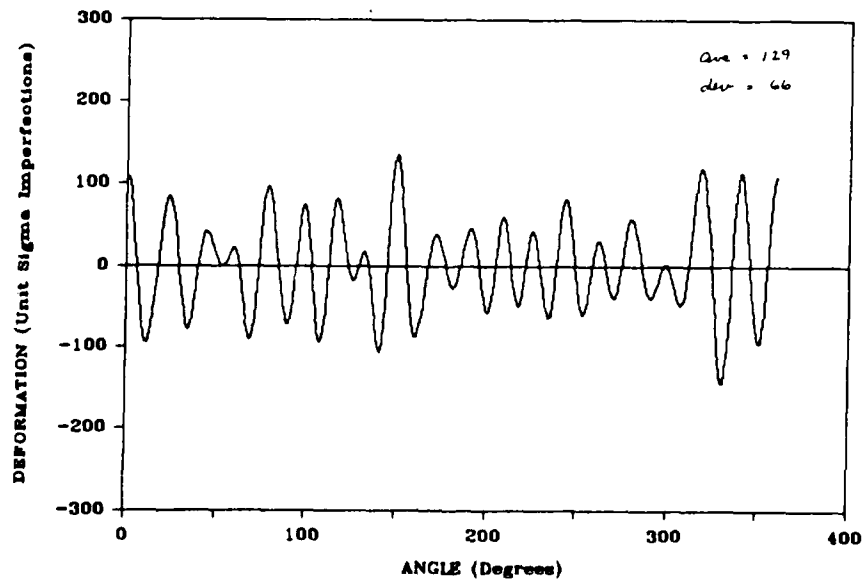
Figure 4.10: Buckle shape from white-noise imperfections, $s = 20.67$, $\tau = 6$, case 8.
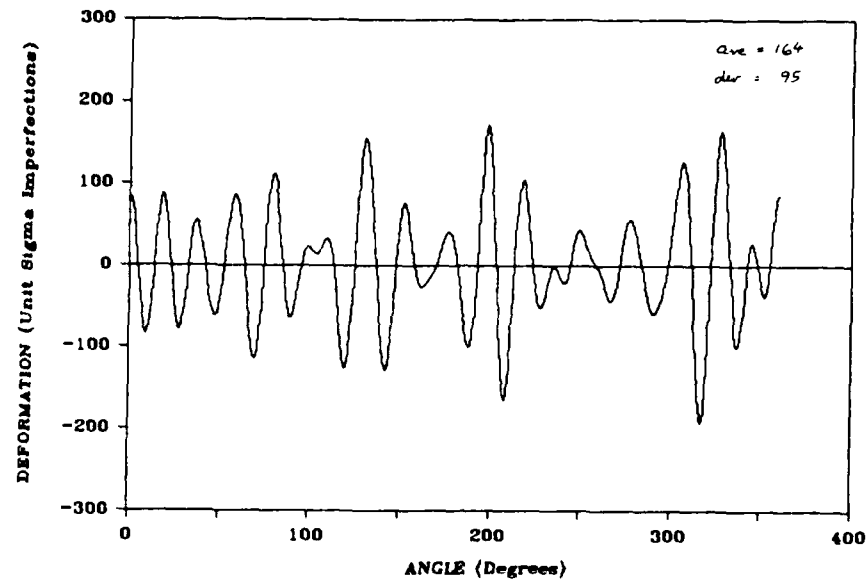
Figure 4.11: Buckle shape from white-noise imperfections, $s = 20.67$, $\tau = 6$, case 9.
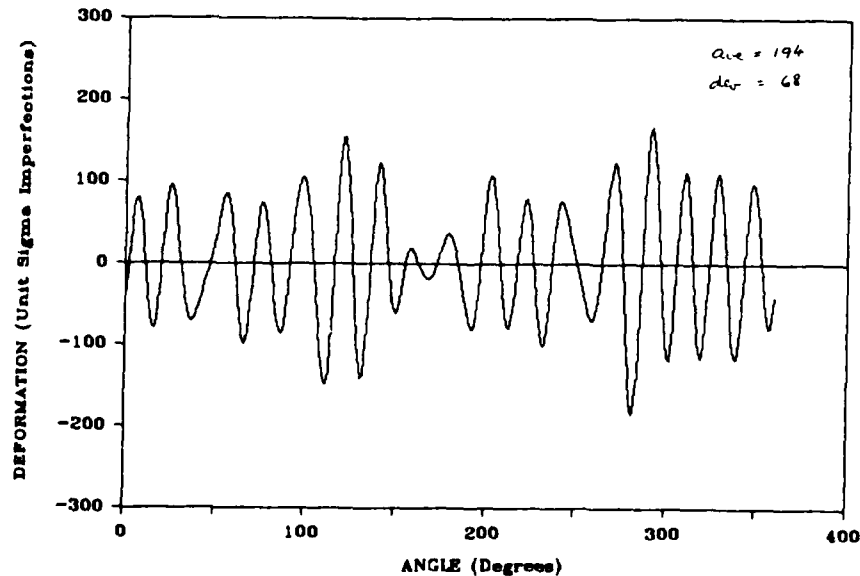

Figure 4.12: Buckle shape from white-noise imperfections, $s = 20.67$, $\tau = 6$, case 10.

39
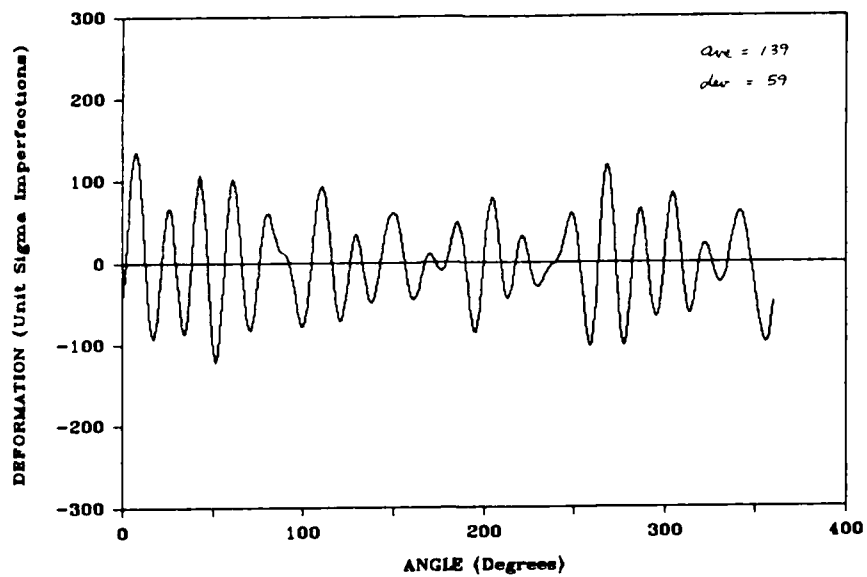
Figure 4.13: Buckle shape from white-noise imperfections, $s = 20.67$, $\tau = 6$, case 11.
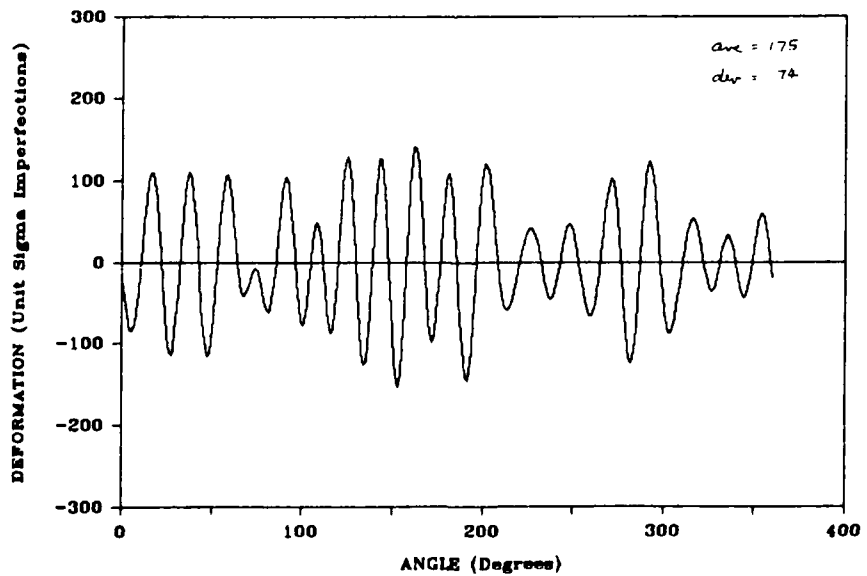
Figure 4.14: Buckle shape from white-noise imperfections, $s = 20.67$, $\tau = 6$, case 12.

40
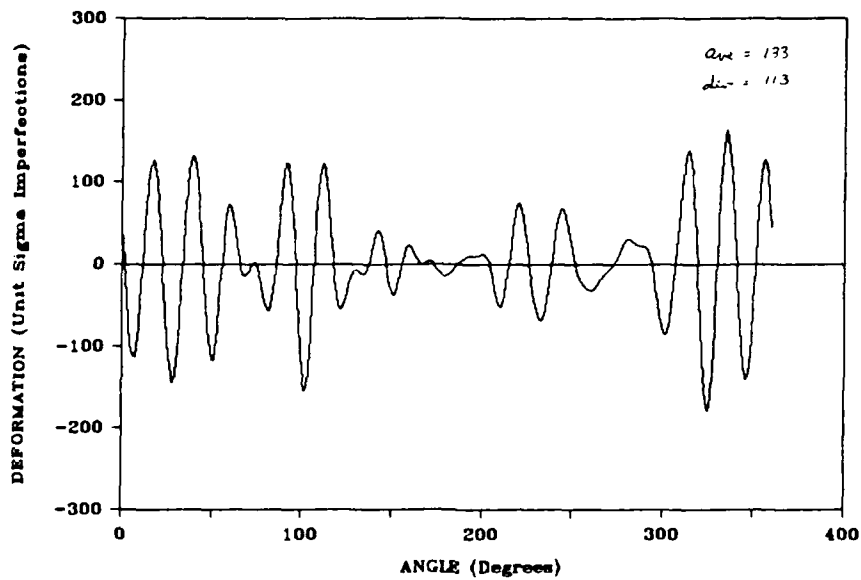
Figure 4.15: Buckle shape from white-noise imperfections, $s = 20.67$, $\tau = 6$, case 13.
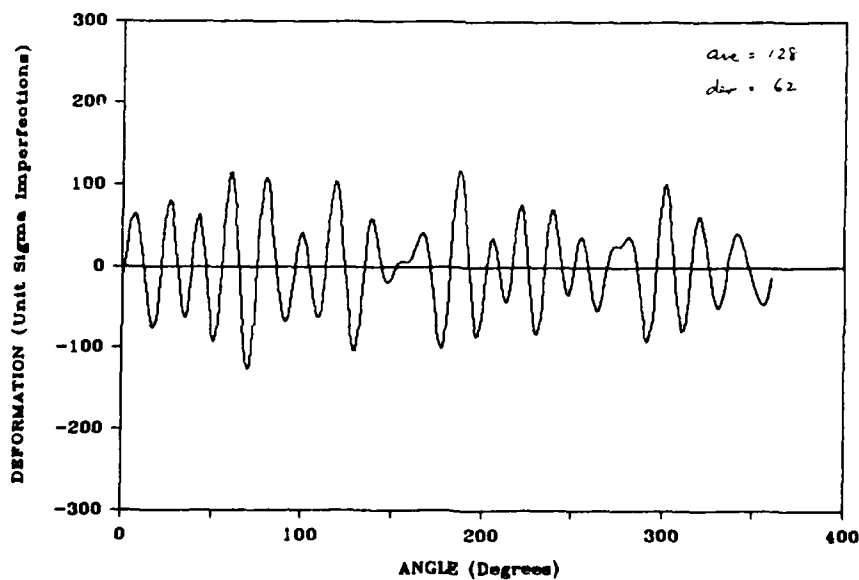
Figure 4.16: Buckle shape from white-noise imperfections, $s = 20.67$, $\tau = 6$, case 14.

41
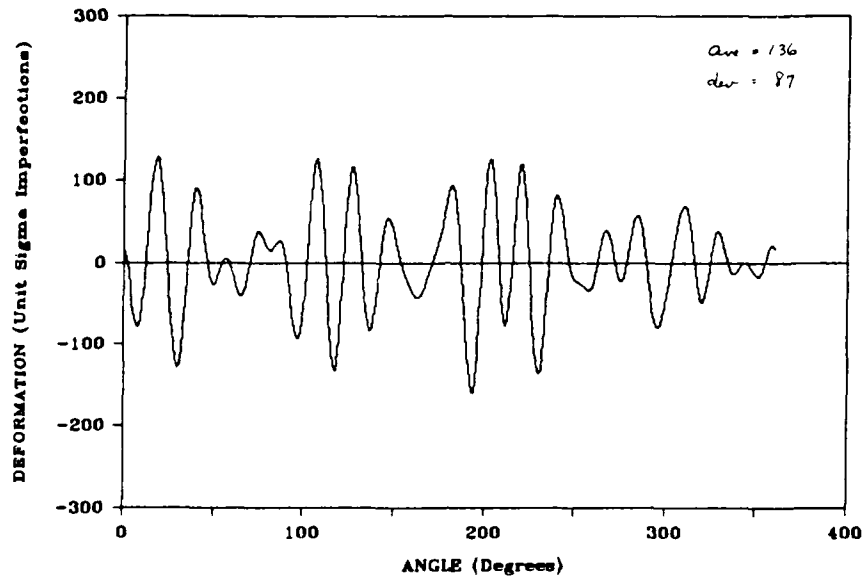
Figure 4.17: Buckle shape from white-noise imperfections, $s = 20.67$, $\tau = 6$, case 15.
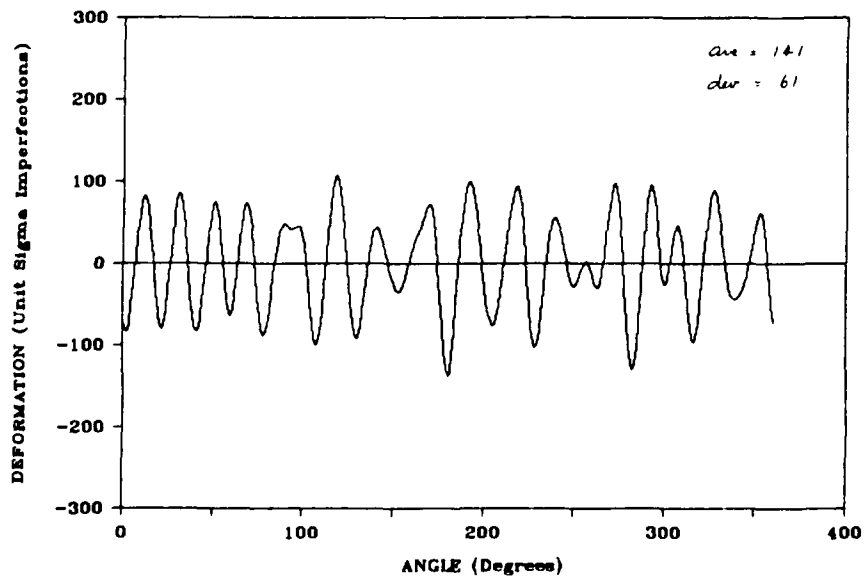
Figure 4.18: Buckle shape from white-noise imperfections, $s = 20.67$, $\tau = 6$, case 16.

42
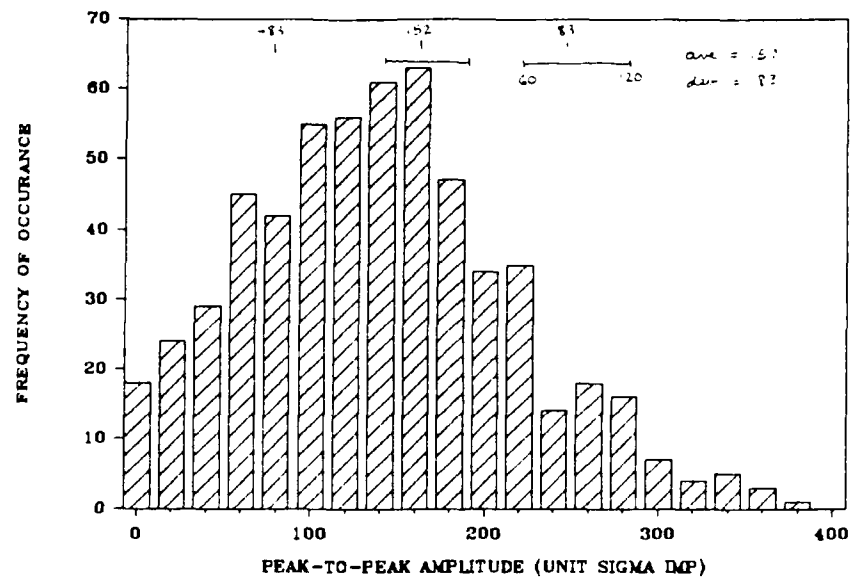
Figure 4.19: Histogram of buckle amplitude distribution, $s = 20.67$, $\tau = 6$, unit imperfection coefficients.
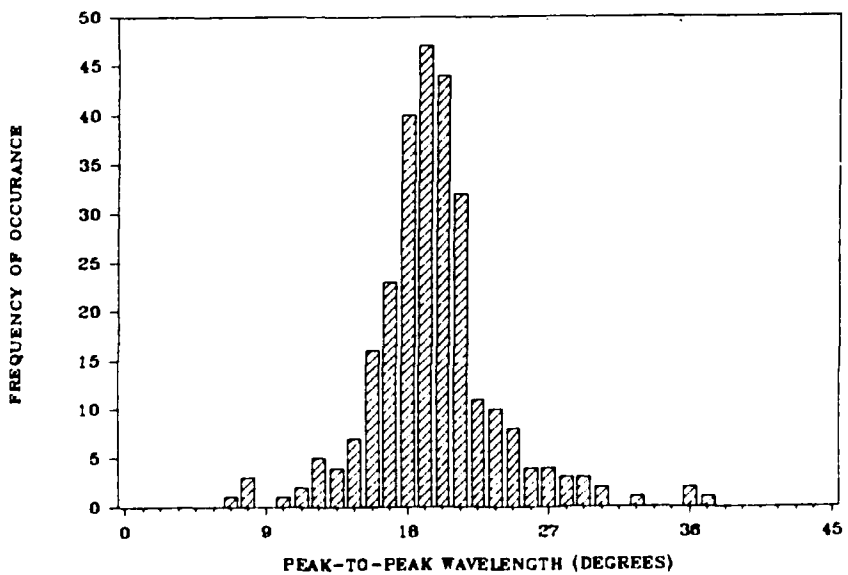
Figure 4.20: Histogram of buckle wavelength distribution, $s = 20.67$, $\tau = 6$, unit imperfection coefficients.

43

44

DISTRIBUTION LIST

DEPARTMENT OF DEFENSE

DEF RSCH & ENGRG
        ATTN: ENGR TECH J PERSCH

DEFENSE ADVANCED RSCH PROJ AGENCY
        ATTN: F PATTON

DEFENSE INTELLIGENCE AGENCY
        ATTN: RTS-2B

DEFENSE NUCLEAR AGENCY
        ATTN: SPAS
        ATTN: SPLH
 4 CYS ATTN: STTI-CA

DEFENSE TECHNICAL INFORMATION CENTER
12 CYS ATTN: DD

STRATEGIC DEFENSE INITIATIVE ORGANIZATION
        ATTN: P TERRY
        ATTN: R YESENSKY
        ATTN: S GEARY

DEPARTMENT OF THE ARMY

U S ARMY MATERIAL TECHNOLOGY LABORATORY
        ATTN: R FITZPATRICK

U S ARMY STRATEGIC DEFENSE COMMAND
        ATTN: SDC/S BROCKWAY

US ARMY MISSILE COMMAND
        ATTN: W FRIDAY

DEPARTMENT OF THE NAVY

NAVAL INTELLIGENCE SUPPORT CTR
        ATTN: NISC-11 A COBLEIGH

NAVAL POSTGRADUATE SCHOOL
        ATTN: PROF K E WOEHLER, CODE 61WH

NAVAL RESEARCH LABORATORY
        ATTN: CODE 4600 D NAGEL
        ATTN: CODE 4633 R WENZEL

NAVAL SEA SYSTEMS COMMAND
 2 CYS ATTN: PMS
        ATTN: R RUDKIN

NAVAL SURFACE WEAPONS CENTER
        ATTN: CODE R-31 J THOMPSON

OFFICE OF NAVAL TECHNOLOGY
        ATTN: CODE 217

STRATEGIC SYSTEMS PROGRAM OFFICE (PM-1)
        ATTN: NSP-L63 (TECH LIB)

DEPARTMENT OF THE AIR FORCE

AIR FORCE CTR FOR STUDIES & ANALYSIS
        ATTN: AFCSA/SAMI (R GRIFFIN)

AIR FORCE SYSTEMS COMMAND
        ATTN: DLWM

AIR FORCE WEAPONS LABORATORY, AFSC
        ATTN: E HERRERA
        ATTN: NTCO C AEBY
        ATTN: TA B FREDERICKSON
        ATTN: TA J WALTON
        ATTN: TALE T EDWARDS

AIR FORCE WRIGHT AERONAUTICAL LAB
        ATTN: AFWAL/MLP W WOODY
        ATTN: B LAINE
     . ATTN: J RHODEHAMEL
        ATTN: MLPJ/DR S R LYON
        ATTN: W HARRIS

FOREIGN TECHNOLOGY DIVISION, AFSC
        ATTN: A CORDOVA

SPACE DIVISION/YN
        ATTN: YNS D RUBERA

DEPARTMENT OF ENERGY

EG&G IDAHO INC
        ATTN: J EPSTEIN

UNIVERSITY OF CALIFORNIA
LAWRENCE LIVERMORE NATIONAL LAB
        ATTN: F SERDUKE
        ATTN: L-10 W BOOKLESS
        ATTN: L-84 H KRUGER
        ATTN: M GERRISSIMENRO

LOS ALAMOS NATIONAL LABORATORY
        ATTN: B259 MS A GREENE
        ATTN: C931 MS T KING
        ATTN: E548 R S DINGUS
        ATTN: J PORTER

SANDIA NATIONAL LABORATORIES
        ATTN: M BIRNBAUM

SANDIA NATIONAL LABORATORIES
        ATTN: DR J POWELL
        ATTN: K MATZEN

DEPARTMENT OF DEFENSE CONTRACTORS

ACUREX CORP
        ATTN: B LAUB

AEROSPACE CORP
ATTN: H BLAES
ATTN: R COOPER
ATTN: T PARK

APTEK, INC
2 CYS ATTN: H LINDBERG

APTEK, INC
ATTN: DR E FITZGERALD

BATTELLE MEMORIAL INSTITUTE
ATTN: C WALTERS

GENERAL ELECTRIC CO
ATTN: D ENLOW

GENERAL RESEARCH CORP
ATTN: R PARISSE

GENERAL RESEARCH CORP
ATTN: J SOMMERS

HAROLD ROSENBAUM ASSOCIATES, INC
ATTN: G WEBER

JAYCOR
ATTN: DR M TREADAWAY

JAYCOR
ATTN: P SCHALL

KAMAN SCIENCES CORP
ATTN: J CARPENTER
ATTN: R ALMASSY

KAMAN TEMPO
ATTN: DASIAC

KAMAN TEMPO
2 CYS ATTN: DASIAC

KTECH CORP
ATTN: D KELLER

LOCKHEED MISSILES & SPACE CO, INC
ATTN: J PEREZ

MCDONNELL DOUGLAS CORP
ATTN: D JOHNSON
ATTN: J S KIRBY
ATTN: L COHEN

PACIFIC-SIERRA RESEARCH CORP
ATTN: H BRODE, CHAIRMAN SAGE

PHYSICAL SCIENCES, INC
ATTN: A PIRRI

PHYSICS INTERNATIONAL CO
ATTN: C GILMAN
ATTN: J SHEA
ATTN: M KRISHNAN
ATTN: S L WONG

R & D ASSOCIATES
ATTN: B GOULD
ATTN: D GAKENHEIMER
ATTN: F A FIELD
ATTN: P A MILES

RAND CORP
ATTN: E HARRIS

S-CUBED
ATTN: G GURTMAN

SCIENCE APPLICATIONS INTL CORP
ATTN: E TOTON
ATTN: R AIREY
ATTN: S METH
ATTN: W CHADSEY

SCIENCE APPLICATIONS INTL CORP
ATTN: T LAGANELLI

SCIENCE APPLICATIONS INTL CORP
ATTN: H JANEE

SPARTA, INC
ATTN: J E LOWDER
ATTN: R G ROOT

SRI INTERNATIONAL
ATTN: B HOLMES
ATTN: D CURRAN
ATTN: G ABRAHAMSON

TRW ELECTRONICS & DEFENSE SECTOR
ATTN: F FENDELL
ATTN: I RUBIN
ATTN: M SEIZEW

TRW ELECTRONICS & DEFENSE SECTOR
ATTN: W POLICH

VERAC, INC
ATTN: P CARLSON
ATTN: R BINKOWSKI

W J SCHAFER ASSOCIATES, INC
ATTN: J REILLY

END

5-81

DTIC